Waves in one-dimensional quasicrystalline structures: dynamical trace mapping, scaling and self-similarity of the spectrum

Lorenzo Morini and Massimiliano Gei

School of Engineering, Cardiff University,

15-17 The Parade, Cardiff CF24 3AA, Wales, UK.

E-mails: morinil@cardiff.ac.uk, geim@cardiff.ac.uk

June 11, 2018

Abstract

Harmonic axial waves in quasiperiodic-generated structured rods are investigated. The focus is on infinite bars composed of repeated elementary cells designed by adopting generalised Fibonacci substitution rules, some of which represent examples of one-dimensional quasicrystals. Their dispersive features and stop/pass band spectra are computed and analysed by imposing Floquet-Bloch conditions and exploiting the invariance properties of the trace of the relevant transfer matrices. We show that for a family of generalised Fibonacci substitution rules, corresponding to the so-called *precious means*, an invariant function of the circular frequency, the *Kohmoto's invariant*, governs self-similarity and scaling of the stop/pass band layout within defined ranges of frequencies at increasing generation index. Other parts of the spectrum are instead occupied by almost constant *ultrawide* band gaps. The Kohmoto's invariant also explains the existence of particular frequencies, named *canonical* frequencies, associated with closed orbits on the geometrical three-dimensional representation of the invariant. The developed theory represents an important advancement towards the realisation of elastic quasicrystalline metamaterials.

Keywords: generalised Fibonacci sequence, quasiperiodic material, phononic crystal, metamaterial, band gap, Kohmoto's invariant.

1 Introduction

Controlling waves with mechanical metamaterials is an established research field that has reached a certain degree of maturity. Two approaches are mainly followed to achieve the

goal: one is based on the investigation of dispersion properties of periodic structures composed of specifically designed unit or elementary cells (Lin, 1962; Sigalas and Economou, 1992; Kushwaha et al., 1993); the other relies on mathematical transformations that dictate the local features of the metamaterial necessary, for instance, to steer waves along predetermined paths (Milton et al., 2006; Norris, 2008; Brun et al., 2009; Farhat et al., 2009; Parnell et al., 2012; Maldovan, 2013; Colquitt et al., 2014, 2017).

With reference to the first approach, a possible way to conceive the unit cell is that based on quasiperiodic sequences. These are formed by a set of –typically two– homogeneous parts combined to create non-periodic patterns which can be generally described through deterministic rules (commonly known as generation or substitution rules). Depending on the properties of these laws, two distinct classes of quasiperiodic structured media can be identified: *quasicrystalline* structures (Levine and Steinhardt, 1984) and *non-quasicrystalline* deterministic systems (Huang et al., 1992). In the one-dimensional setting, a rigorous method of classification for the different quasiperiodic patterns was proposed by Kolar (1993). Based on this criterion, we define a one-dimensional quasiperiodic chain composed of two distinct elements, say L and S, generated according to the generic substitution rule

$$L \to \varsigma(L) = \mathcal{M}_{\alpha\beta}(L,S), \quad S \to \varsigma(S) = \mathcal{N}_{\gamma\delta}(L,S), \tag{1}$$

where $\mathcal{M}_{\alpha\beta}(L,S)$ and $\mathcal{N}_{\gamma\delta}(L,S)$ are two building blocks consisting of a certain permutation of $\alpha+\beta$ and $\gamma+\delta$ elements, respectively. Parameters α and β denote the number of elements L and S in $\varsigma(L)$, respectively, whilst γ and δ are their counterpart in $\varsigma(S)$. Introducing the structure parameter $w = \beta\gamma - \alpha\delta$, the condition for having a quasicrystalline system is $w = \pm 1$. Quasicrystalline media possess very peculiar characteristics that make them an intermediate class of structured materials between periodic ordered crystals and random media (Steurer, 2004; Steurer and Deloudi, 2008). A typical example of one-dimensional quasicrystalline pattern is represented by the Fibonacci *golden* sequence for which $\alpha = \beta = \gamma = 1$ and $\delta = 0$, while in plane problems an example of a quasicrystalline tessellation is the Penrose tiling (Penrose, 1974). Conversely, an example of non-quasicrystalline deterministic system whose properties are more similar to those of a random media is represented by the so-called Thue-Morse chain (Tamura and Nori, 1989).

The electromagnetic behaviour of one-dimensional quasicrystalline electronic, optical and magnetic media has been extensively studied both theoretically (Kohmoto et al., 1983, 1987; Kolar and Ali, 1989b) and experimentally (Laruelle and Etienne, 1988). All these investigations have shown that although quasicrystalline systems are not periodic, their features can be described using quasiperiodic approximants. Moreover, their electronic and optical spectra possess a self-similar ordered layout characterised by scaling laws which cannot be observed in periodic or purely random media (Kohmoto and Oono, 1984).

In mechanics, despite a few attempts to study dispersion properties of elastic Fibonacci-generated waveguides (King and Cox, 2007; Gei, 2010; Zhao et al., 2013), the understanding of these scaling phenomena has not yet been satisfactorily addressed for quasicrystalline and general quasiperiodic structures. An investigation is therefore required to reveal the basic features of dynamic spectra and provide the necessary guidelines for their possible exploitation in the design of novel architectured materials whose stop and pass band topology can be easily modulated and controlled.

In this paper, waves in one-dimensional phononic quasicrystalline systems for applications in structural mechanics are thoroughly studied. In particular, our goals are:

- to provide a general framework to analyse axial harmonic wave propagation of quasicrystalline generalised Fibonacci rods;
- to highlight the role of trace mapping and that of an invariant function, the Kohmoto's invariant, in determining the properties of harmonic dynamics of such structures;
- to study the scaling properties of the dynamic spectra exploiting the features of the Kohmoto's invariant;
- to investigate the occurrence of *ultrawide* stop bands occurring in the dynamic spectra;
- to introduce a special class of quasicrystalline structures, named *canonical* structures, that display special conservation properties in the stop/pass band diagram.

The outcome of this paper sets out a methodology to be applied to the mechanics of quasicrystalline-generated beams, plates and composite materials.

2 One-dimensional generalised Fibonacci structures

We introduce a particular class of infinite, one-dimensional, bi-component quasiperiodic structures. Its elements are composed of a repeated elementary cell where two distinct elements, say L and S, which can be springs, rods or supported beams, are arranged in series according to the generalised Fibonacci sequence (Poddubny and Ivchenko, 2010). The repetition of such quasiperiodic fundamental cells implies global periodicity along the axis and then the possibility of applying the Floquet-Bloch technique in order to study harmonic wave propagation in these systems. The generalised two-component Fibonacci sequence is based on the following substitution rule (Kolar and Ali, 1989b):

$$L \to \varsigma(L) = L^m S^\ell, \;\; S \to \varsigma(S) = L, \quad \text{with } m,\, \ell \geq 1, \tag{2}$$

where the exponent indicates the times the base is repeated, i.e. $L^m = LLL\ldots$ (m times). In terms of the general definition (1), the parameters of the substitutive relation

(2) are given by $\alpha = m,\ \beta = \ell,\ \gamma = 1,\ \delta = 0$ and $w = \ell$. Expression (2) implies that the finite generalised Fibonacci sequence of the $i-$th order ($i = 0, 1, 2, \dots$), here denoted by $\mathcal{F}_i$, obeys the recursive rule

$$\mathcal{F}_i = \mathcal{F}_{i-1}^m \mathcal{F}_{i-2}^\ell, \quad \text{with } m,\, \ell \geq 1, \tag{3}$$

where the initial conditions are $\mathcal{F}_0 = S$ and $\mathcal{F}_1 = L$. The total number of elements of $\mathcal{F}_i$ corresponds to the generalised Fibonacci number $\tilde{n}_i$ given by the recurrence relation

$$\tilde{n}_i = m\tilde{n}_{i-1} + \ell\tilde{n}_{i-2}, \quad \text{with } i \geq 2, \tag{4}$$

and $\tilde{n}_0 = \tilde{n}_1 = 1$. The limit σ of the ratio $\tilde{n}_{i+1}/\tilde{n}_i$ for $i \to \infty$ is

$$\sigma = \lim_{i\to\infty} \frac{\tilde{n}_{i+1}}{\tilde{n}_i} = \frac{m + \sqrt{m^2 + 4\ell}}{2}. \tag{5}$$

The standard Fibonacci sequence is obtained from the substitution rule (2) setting $m = \ell = 1$, for which σ corresponds to the *golden* mean (GM) $\sigma = \sigma_g = (1 + \sqrt{5})/2 \cong 1.618$, and the recurrence relation (4) becomes the expression for the Fibonacci number $n_i = n_{i-1} + n_{i-2}$ ($i \geq 2$). The structures generated assuming $m = 2$ and $\ell = 1$ are the so-called *silver* mean (SM) chains, whose limit (5) corresponds to the *silver* mean $\sigma = \sigma_s = (1+\sqrt{2}) \cong 2.414$, whereas for $m = 3$ and $\ell = 1$ the *bronze* mean (BM) recursion rule is obtained with $\sigma = \sigma_b = (3 + \sqrt{13})/2 \cong 3.303$. Generalised Fibonacci structures realised setting $m = 1,\ \ell = 2$ and $m = 1,\ \ell = 3$ are commonly known respectively as *copper* and *nickel* mean chains, and their application to the modelling of quasiperiodic electronic and magnetic systems has also been studied (Gumbs and Ali, 1988; Kolar and Ali, 1989a). The limit (5) of the former is the *copper* mean $\sigma = \sigma_c = 2$, whereas that of the latter is the *nickel* mean $\sigma = \sigma_n = (1 + \sqrt{13})/2 \cong 2.302$.

We observe that σ_g, σ_s and σ_b correspond to the first three terms of the continuative fraction whose parametric representation can be defined by setting $\ell = 1$ in expression (5). Further in the text, adopting the nomenclature proposed by Holzer (1988a,b), we will refer to these values as *precious* means and call collectively the associated structures *precious mean structures*. Specularly, σ_c, σ_n and all values of ratio (5) obtained assuming $\ell > 1$ will be referred to as *metal* means, and the corresponding structures will be called *metal mean structures*. By remembering the general criterion introduced by Kolar (1993) reported in the Introduction, it is important to note that for all *precious mean structures* we have $w = \ell = 1$, while for *copper* and *nickel* mean structures $w = \ell = 2$ and $w = \ell = 3$, respectively. Therefore, the former are quasicrystalline, whereas the latter group are deterministic non-quasicrystalline, quasiperiodic systems.

3 Axial waves in a quasicrystalline rod

The focus of the paper is on axial waves in quasicrystalline waveguides, however the content of this section is also valid for more general quasiperiodic-generated rods. Let us

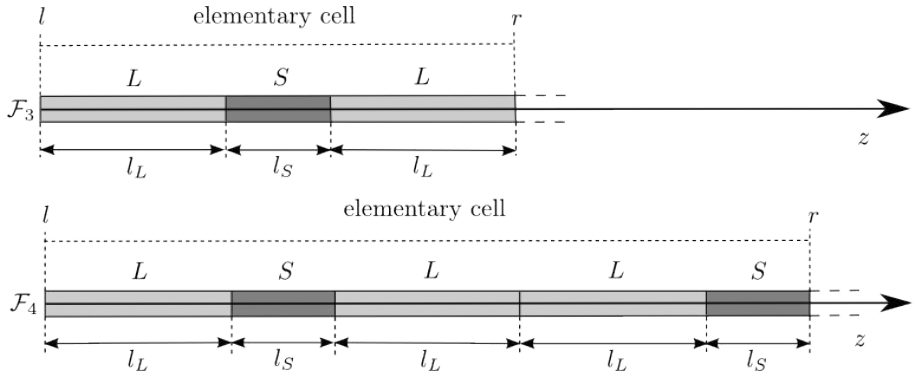

Figure 1: Axial waves in a quasicrystalline structured rod: elementary cells for infinite structures based on Fibonacci GM chains $\mathcal{F}_3 = (LSL)$ (top) and $\mathcal{F}_4 = (LSLLS)$ (bottom). Symbols r and l denote respectively right and left-hand boundaries of the cell.

consider then a quasiperiodic bi-phase structured rod whose elementary cell is generated adopting the generalised Fibonacci sequences (in Fig. 1, the GM sequences $\mathcal{F}_3$ and $\mathcal{F}_4$ are displayed)[1]. The lengths of the two segments L and S are indicated respectively with l_L and l_S, while A_X, E_X, and ρ_X ($X \in \{L, S\}$) denote cross-section area, Young's modulus and mass density per unit length of each element, respectively.

For both elements, we define the displacement function along the rod $u(z)$ and the axial force $N(z) = EAu'(z)$, where z is the longitudinal axis. The field equation of harmonic waves assumes the form

$$u''(z) + Q\,\omega^2 u(z) = 0, \tag{6}$$

where $Q = \rho/EA$, ω is the circular frequency (simply the 'frequency' in the following), and the solution is given by

$$u(z) = C_1 \sin(\sqrt{Q}\,\omega z) + C_2 \cos(\sqrt{Q}\,\omega z). \tag{7}$$

It is worth pointing out that eq. (6) is the one-dimensional Helmholtz equation which governs several dynamics problems in solid mechanics such as shear waves in antiplane elasticity and in-plane compressional and shear waves in two-dimensional elasticity (see Ewing et al. (1956); Graff (1975)).

To obtain the dispersion diagram of the periodic rod, displacement and the axial force at the right-hand boundary of the elementary cell, respectively u_r and N_r, have to be given in terms of those at the left-hand boundary, u_l and N_l, as

$$\boldsymbol{U}_r = \boldsymbol{T}_i\,\boldsymbol{U}_l, \tag{8}$$

[1]Henceforth, the notation $\mathcal{F}_i$ will indicate both the sequence and the elementary cell of the structured rod.

where $\boldsymbol{U}_j = [u_j \;\; N_j]^T$ $(j = r, l)$ and $\boldsymbol{T}_i$ is a transfer (or transmission) matrix of the cell $\mathcal{F}_i$. This matrix is the result of the product $\boldsymbol{T}_i = \prod_{p=1}^{\tilde{n}_i} \boldsymbol{T}^X$, where $\boldsymbol{T}^X$ $(X \in \{L, S\})$ is the transfer matrix relating quantities across a single element given by

$$\boldsymbol{T}^X = \begin{bmatrix} \cos(\sqrt{Q_X}\,\omega l_X) & \dfrac{\sin(\sqrt{Q_X}\,\omega l_X)}{E_X A_X \sqrt{Q_X}\,\omega} \\ -E_X A_X \sqrt{Q_X}\,\omega \sin(\sqrt{Q_X}\,\omega l_X) & \cos(\sqrt{Q_X}\,\omega l_X) \end{bmatrix}. \tag{9}$$

Matrices $\boldsymbol{T}_i$ have some important properties that can be exploited: i) they are unimodular, i.e. $\det \boldsymbol{T}_i = 1$, and ii) follow the recursion rule

$$\boldsymbol{T}_{i+1} = \boldsymbol{T}_{i-1}^{\ell}\, \boldsymbol{T}_i^{m}, \tag{10}$$

with $\boldsymbol{T}_0 = \boldsymbol{T}^S$ and $\boldsymbol{T}_1 = \boldsymbol{T}^L$.

The Floquet-Bloch condition requires that $\boldsymbol{U}_r = \exp(iK)\,\boldsymbol{U}_l$ (here i denotes the imaginary unit), so that, combining this with (8), the dispersion equation takes the form

$$\det[\boldsymbol{T}_i - e^{iK}\boldsymbol{I}] = 0. \tag{11}$$

The solution of the dispersion relation (11) provides the complete Floquet-Bloch spectrum, and allows to obtain the stop/pass band distribution associated with the quasiperiodic rods here considered (stop bands are also named band gaps throughout the paper).

Alternatively, we can study the dispersion properties of these structures by evaluating the eigenvalues of the transfer matrix. As $\boldsymbol{T}_i$ is unimodular, it turns out that the characteristic equation of the quasiperiodic rod is given by

$$\det[\boldsymbol{T}_i - \lambda\boldsymbol{I}] = 0 \quad \Rightarrow \quad \lambda^2 - \lambda\,\mathsf{tr}\,\boldsymbol{T}_i + 1 = 0. \tag{12}$$

Substituting $e^{iK} = \lambda$ in eq. (12) and multiplying it by e^{-iK}, the condition $e^{iK} + e^{-iK} - \mathsf{tr}\,\boldsymbol{T}_i = 0$ is achieved, leading to $2\cos K - \mathsf{tr}\,\boldsymbol{T}_i = 0$, and finally to the alternative expression for the dispersion relation

$$K = \arccos\left(\frac{\mathsf{tr}\,\boldsymbol{T}_i}{2}\right), \tag{13}$$

that is a real quantity if $|\mathsf{tr}\,\boldsymbol{T}_i| \leq 2$. By observing eq. (13), we can easily deduce that all the information concerning wave propagation in a structure whose elementary cell is generated according to the arbitrary sequence $\mathcal{F}_i$ is contained in the trace $\mathsf{tr}\,\boldsymbol{T}_i$ of the corresponding transfer matrix.

The transfer matrix method has been extensively used to study the dynamics of periodic laminates (Willis, 2016), multilayered materials with structured interfaces (Brun et al., 2010) and phononic crystals (Wu et al., 2009; Nemat-Nasser et al., 2015). It has been extended to multi-phase flexural systems by Romeo and Luongo (2002); Carta and Brun (2015); Shmuel and Pernas-Salomon (2016).

4 Dynamical trace mapping for precious mean structures

In this Section we analyse the properties of the trace $\mathsf{tr}\,\boldsymbol{T}_i$ associated with *precious* mean sequences, and discuss how these features affect waves in *precious* mean structures. Nonlinear recursive relationships connecting those traces for consecutive sequences are derived. Through the linearisation of these maps, analytical scaling factors which govern self-similarity of stop and pass band pattern of *golden*, *silver* and *bronze* mean structures (GMSs, SMSs and BMSs, respectively) will be obtained.

4.1 Nonlinear maps and Kohmoto's invariant

General recursive relations for the traces of unimodular 2×2 transfer matrices of generalised Fibonacci chains have been derived by Kolar and Ali (1989b) and Kolar and Nori (1990) in terms of Chebyshev polynomials of first and second kind. Specialising these expressions to the case of GMSs ($m = \ell = 1$ in eq. (10)), we derive the following recursive rule

$$x_{i+1} = x_{i-1}x_i - x_{i-2}, \quad \text{with} \;\; i \geq 2, \tag{14}$$

where we have introduced the notation $x_i = \mathsf{tr}\,\boldsymbol{T}_i$, and the initial conditions are given by

$$\begin{aligned} x_0 &= 2\cos\left(\sqrt{Q_S}\omega l_S\right), \\ x_1 &= 2\cos\left(\sqrt{Q_L}\omega l_L\right), \\ x_2 &= 2\cos\left(\sqrt{Q_S}\omega l_S\right)\cos\left(\sqrt{Q_L}\omega l_L\right) \\ &\quad -\frac{A_S^2E_S^2Q_S + A_L^2E_L^2Q_L}{A_SE_SA_LE_L\sqrt{Q_SQ_L}}\sin\left(\sqrt{Q_S}\omega l_S\right)\sin\left(\sqrt{Q_L}\omega l_L\right). \end{aligned} \tag{15}$$

Defining $t_i = \mathsf{tr}(\boldsymbol{T}_{i-2}\boldsymbol{T}_{i-1})$, for SMSs ($m = 2$ and $\ell = 1$) the pair of equations

$$\begin{cases} x_{i+1} = x_it_{i+1} - x_{i-1}, \\ t_{i+1} = x_ix_{i-1} - t_i, \end{cases} \quad \text{with} \;\; i \geq 2, \tag{16}$$

are determined; similarly, for BMSs ($m = 3$ and $\ell = 1$),

$$\begin{cases} x_{i+1} = (x_i^2 - 1)t_{i+1} - x_ix_{i-1}, \\ t_{i+1} = x_ix_{i-1} - t_i, \end{cases} \quad \text{with} \;\; i \geq 2. \tag{17}$$

Let us introduce now the new set of variables

$$\tilde{x}_i = t_{i+2}, \;\; \tilde{y}_i = x_{i+1}, \;\; \tilde{z}_i = x_i, \tag{18}$$

where it is important to remember that for GM sequences, $t_{i+2} = \mathsf{tr}(\boldsymbol{T}_i\boldsymbol{T}_{i+1}) = \mathsf{tr}\,\boldsymbol{T}_{i+2} = x_{i+2}$. Substituting coordinates (18) into expression (14), the following nonlinear map determining the evolution of x_i for GMSs is obtained

$$\mathcal{T}_g(\tilde{x}_i, \tilde{y}_i, \tilde{z}_i) = (\tilde{x}_{i+1}, \tilde{y}_{i+1}, \tilde{z}_{i+1}) = (\tilde{x}_i\tilde{y}_i - \tilde{z}_i, \;\; \tilde{x}_i, \;\; \tilde{y}_i). \tag{19}$$

Adopting the same procedure, for SMSs and BMSs we have

$$\mathcal{T}_s(\tilde{x}_i,\tilde{y}_i,\tilde{z}_i)=(\tilde{x}_{i+1},\tilde{y}_{i+1},\tilde{z}_{i+1})=\left(\tilde{x}_i\tilde{y}_i^2-\tilde{y}_i\tilde{z}_i-\tilde{x}_i,\ \tilde{x}_i\tilde{y}_i-\tilde{z}_i,\ \tilde{y}_i\right), \tag{20}$$

and

$$\mathcal{T}_b(\tilde{x}_i,\tilde{y}_i,\tilde{z}_i)=(\tilde{x}_{i+1},\tilde{y}_{i+1},\tilde{z}_{i+1})=\left(\tilde{x}_i\tilde{y}_i^3-\tilde{y}_i^2\tilde{z}_i-2\tilde{x}_i\tilde{y}_i+\tilde{z}_i,\ \tilde{x}_i\tilde{y}_i^2-\tilde{y}_i\tilde{z}_i-\tilde{x}_i,\ \tilde{y}_i\right), \tag{21}$$

respectively. Since (19)–(21) are differentiable maps of the type $\mathcal{T}_{g,s,b}:\mathbb{R}^3\to\mathbb{R}^3$, their Jacobians, namely

$$\boldsymbol{J}=\frac{\partial(\tilde{x}_{i+1},\tilde{y}_{i+1},\tilde{z}_{i+1})}{\partial(\tilde{x}_i,\tilde{y}_i,\tilde{z}_i)}=\begin{bmatrix}\dfrac{\partial\tilde{x}_{i+1}}{\partial\tilde{x}_i} & \dfrac{\partial\tilde{x}_{i+1}}{\partial\tilde{y}_i} & \dfrac{\partial\tilde{x}_{i+1}}{\partial\tilde{z}_i}\\ \dfrac{\partial\tilde{y}_{i+1}}{\partial\tilde{x}_i} & \dfrac{\partial\tilde{y}_{i+1}}{\partial\tilde{y}_i} & \dfrac{\partial\tilde{y}_{i+1}}{\partial\tilde{z}_i}\\ \dfrac{\partial\tilde{z}_{i+1}}{\partial\tilde{x}_i} & \dfrac{\partial\tilde{z}_{i+1}}{\partial\tilde{y}_i} & \dfrac{\partial\tilde{z}_{i+1}}{\partial\tilde{z}_i}\end{bmatrix}, \tag{22}$$

can be evaluated showing that for all the three maps $\det\boldsymbol{J}=-1$. Through a little algebra we can also demonstrate that the quantity

$$I(\omega)=\tilde{x}_i^2+\tilde{y}_i^2+\tilde{z}_i^2-\tilde{x}_i\tilde{y}_i\tilde{z}_i-4=$$

$$=\frac{(A_L^2E_L^2Q_L-A_S^2E_S^2Q_S)^2}{A_S^2E_S^2A_L^2E_L^2Q_SQ_L}\sin^2\left(\sqrt{Q_S}\omega l_S\right)\sin^2\left(\sqrt{Q_L}\omega l_L\right) \tag{23}$$

is an invariant for all the three maps. This means that, for *precious* mean rods, at a given frequency ω, the value $I(\omega)$ is independent of the order i of the sequence $\mathcal{F}_i$. In the three-dimensional space spanned by the orthogonal system $O\tilde{x}\tilde{y}\tilde{z}$,

$$\tilde{x}^2+\tilde{y}^2+\tilde{z}^2-\tilde{x}\tilde{y}\tilde{z}-4=I(\omega) \tag{24}$$

is the cartesian equation of a two-dimensional manifold, then it is a surface. The points obtained by iterating maps (19)–(21) are all confined on this surface. Consequently, for any given frequency ω, all points, detected by the triad $R_i=(\tilde{x}_i,\tilde{y}_i,\tilde{z}_i)$ and generated through (19)–(21) can be mapped onto a surface defined by eq. (24). For GM rods, all three coordinates $\tilde{x}_i$, $\tilde{y}_i$ and $\tilde{z}_i$ represent values of traces corresponding to three 'adjacent' sequences. Conversely, for SM and BM, $\tilde{x}_i=\mathsf{tr}(\boldsymbol{T}_i\boldsymbol{T}_{i+1})$ is an auxiliary variable introduced respectively in the recurrence relations (16) and (17), therefore only $\tilde{y}_i=x_{i+1}$ and $\tilde{z}_i=x_i$ refer to traces of transfer matrices and can be mapped on the curve obtained by the intersection between the surface (24) and the plane $\tilde{x}_i=0$.

The sets of points generated iterating maps (19)–(21) define orbits which are also fully confined on the surface (24). This surface was first introduced by Kohmoto and

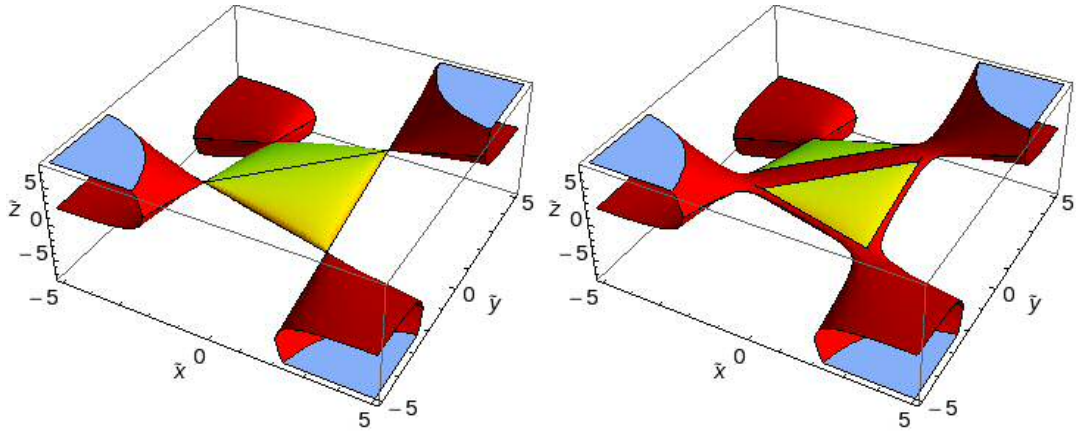

Figure 2: Kohmoto's manifolds for GM rods for $\sqrt{Q_L}\omega l_L = 0.1$ (on the left) and $\sqrt{Q_L}\omega l_L = 3\pi/2$ (on the right). Yellow surfaces denote loci of points for which $\{|\tilde{x}|, |\tilde{y}|, |\tilde{z}|\} \leq 2$. Red ones denote loci of points for which the frequency is in a band gap for at least one of the cells $\mathcal{F}_{i+2}$, $\mathcal{F}_{i+1}$ and $\mathcal{F}_i$ (i.e. at least one of the inequalities $|\tilde{x}_i| \geq 2$, $|\tilde{y}_i| \geq 2$ and $|\tilde{z}_i| \geq 2$ is satisfied).

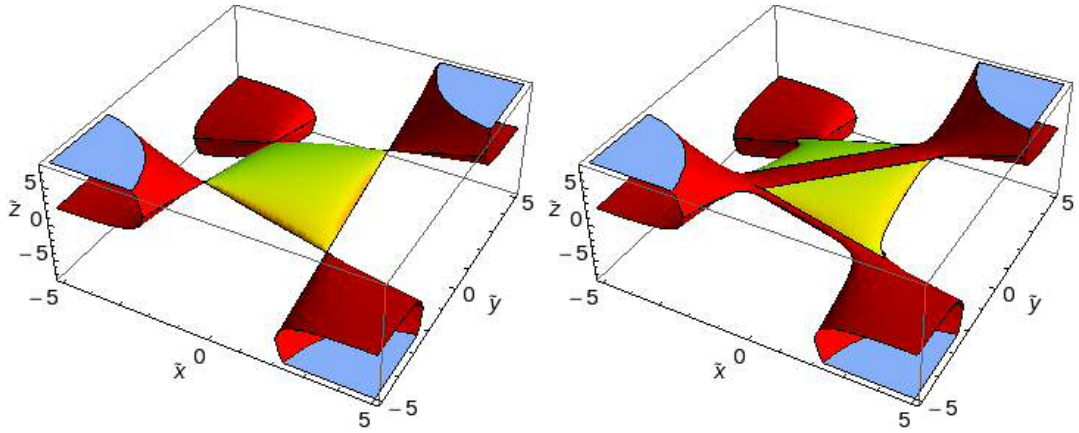

Figure 3: Kohmoto's manifolds for SM rods for $\sqrt{Q_L}\omega l_L = 0.1$ (on the left) and $\sqrt{Q_L}\omega l_L = 3\pi/2$ (on the right). The yellow regions denote loci of points for which $\{|\tilde{y}|, |\tilde{z}|\} \leq 2$. Red ones denote loci of points for which the frequency is in a band gap for at least one of the cells $\mathcal{F}_{i+1}$ and $\mathcal{F}_i$ (i.e. either $|\tilde{y}_i| \geq 2$ or $|\tilde{z}_i| \geq 2$ –or both– is satisfied).

Oono (1984) while investigating the spectrum of Schrödinger equations in quasiperiodic potential wells generated according to the GM rule. In recognition of the contribution to the field by M. Kohmoto, $I(\omega)$ will be called Kohmoto's invariant and the surface (24) Kohmoto's surface or manifold.

Two examples of the manifold defined by eq. (24) are shown in Fig. 2 for GMSs ($\rho_L/\rho_S = 2$, $l_L/l_S = \sigma_g$, $E_S = E_L$ and $A_S = A_L$), for the normalised frequencies $\sqrt{Q_L}\omega l_L = 0.1$ and $3\pi/2$. In each chart, we have highlighted in yellow portions of the surface belonging to the three-dimensional interval $\{|\tilde{x}|, |\tilde{y}|, |\tilde{z}|\} \leq 2$, while the red areas represent parts of the surface where at least one of the inequalities $|\tilde{x}| \geq 2$, $|\tilde{y}| \geq 2$

and $|\tilde{z}| \geq 2$ is satisfied. Taking eq. (13) as a reference, on the one hand, if a point $R_i = (\tilde{x}_i, \tilde{y}_i, \tilde{z}_i)$ lies on a yellow zone, at this frequency waves propagate along all the three rods composed of the three elementary cells $\mathcal{F}_i$, $\mathcal{F}_{i+1}$ and $\mathcal{F}_{i+2}$ (the frequency belongs to a pass band for all the three sequences). On the other hand, if R_i belongs to a red region, for at least one of the three elementary cells described by its coordinates the investigated frequency lies on a band gap. In Fig. 3, Kohmoto's surfaces corresponding to SMSs are reported for the same normalised frequencies and constitutive parameters assumed for the GM case. In analogy with Fig. 2, we have highlighted in yellow portions of the manifolds for which $|\tilde{y}| \leq 2$ and $|\tilde{z}| \leq 2$, while in red those for which both or at least one of the following inequalities, $|\tilde{y}| \geq 2$ and $|\tilde{z}| \geq 2$, is satisfied. In this case, if a point $R_i = (\tilde{x}_i, \tilde{y}_i, \tilde{z}_i)$ lies on a yellow zone, at this frequency waves propagate along both the two rods generated by $\mathcal{F}_i$ and $\mathcal{F}_{i+1}$. Conversely, if the point belongs to a red region, for at least one of the two elementary cells described by the coordinates $\tilde{z}_i$ and $\tilde{y}_i$ the investigated frequency is in a band gap. The difference in the use of the Kohmoto's surface to illustrate the propagation and band gap regions in GMSs and SMSs is given by the fact that for SM (and BM) cases the coordinate $\tilde{x}_i$ does not represent the trace of a transfer matrix, and then, differently from $|\tilde{y}| \geq 2$ and $|\tilde{z}| \geq 2$, the condition $|\tilde{x}| \geq 2$ is not associated with a band gap of a structure generated using this sequence.

We note that the quantity (23) plays an important role also for *metal mean* quasiperiodic structures. For these, which can be described by non-conservative maps (Kolar and Ali, 1990), $I(\omega)$ represents a pseudo-invariant and the surface corresponding to $I(\omega) = 0$ is an *attractor*.

4.2 Orbits on Kohmoto's surface

Using the terminology provided by renormalization theory (Kohmoto and Oono, 1984), the maps (19)–(21) can be regarded as 'scale transformations'. As we have just discussed, at a given circular frequency ω, the orbits given by the successive iterations are confined on the surface uniquely determined by the values of $I(\omega)$. As a consequence, $I(\omega)$ is a 'scale invariant' of the model.

With reference to all *precious* mean rods, there are four kinds of orbits which can be followed increasing the index of variables (18) on the Kohmoto's surface:

a) periodic orbits;

b) non-periodic bounded orbits;

c) escaping orbits with $\lim_{i\to\infty} |x_i| \leq 2$;

d) fully escaping orbits with $\lim_{i\to\infty} |x_i| > 2$, where x_i represents a generic coordinate $\tilde{x}_i$, $\tilde{y}_i$ or $\tilde{z}_i$ for GM rods, and $\tilde{y}_i$ or $\tilde{z}_i$ for both SM and BM counterparts.

The type of orbit is uniquely determined by the initial point $R_0 = (\tilde{x}_0, \tilde{y}_0, \tilde{z}_0)$. In detail, if the orbit is periodic [case a)], after a certain number N of iterations the triple $(\tilde{x}_i, \tilde{y}_i, \tilde{z}_i)$ assumes again the values of the initial point R_0, and then for this value of ω the same sequence of stop and pass bands is observed every N iterations. Differently,

non-periodic bounded orbits [case b)] are relative to cases where R_i never assumes the initial position again at increasing index, and then the trajectory defined by the successive points is open, remaining confined to the central body of the Kohmoto's surface (see Fig. 2) without reaching the lateral tails of the manifold at any iteration.

Concerning the escaping cases, if the orbit is fully escaping [case d)], x_i increases at each iteration and the orbits evolve on the lateral tails of the manifold, sketched in red in Fig. 2. Therefore, the value of ω associated with the Kohmoto's surface is here in a band gap for all rods of the sequence beyond a certain index i. Conversely, if the orbit is simply escaping [case c)], $|x_i|$ assumes values alternatively greater and lesser than 2. As a consequence, for a given frequency ω it is possible to have some cells in a band gap followed by others where, instead, waves are transmitted.

The connection between orbits on the Kohmoto's surfaces generated by iterating maps (19)–(21) and the stop/pass band diagrams is illustrated in Fig. 4 for three prototype waveguides. In Fig. 4/*a*), the stop/pass band pattern of GM sequences $\mathcal{F}_2$ to $\mathcal{F}_7$ is illustrated for $l_S = l_L/\sigma_g$ and $\rho_S = \rho_L/2$ (pass band: blue line; stop band: white gap). The three values of the normalised frequency $\sqrt{Q_L}\omega l_L = 0.15, 1.25, 2.5$, respectively indicated as b), c) and d) consistently with labels of the remaining three charts of the same figure, are identified using vertical red lines. The Kohmoto's surfaces corresponding to these values of the normalised frequency are shown respectively in Figs. 4/*b*), /*c*) and /*d*). The sketched black dots denote the points $R_i = (\tilde{x}_i, \tilde{y}_i, \tilde{z}_i) = (x_{i+2}, x_{i+1}, x_i)$ mapped on the surface for the first iterations of the transformation (19). It is observed that each of the three cases displays a different type of trajectory due to the different initial condition R_0. With reference to Fig. 4/*a*), it is important to note that the portion Ω of the spectrum occupied by band gaps increases monotonically at increasing index i. For our prototype structure, Ω goes from 0.8428 for $\mathcal{F}_2$ to 1.2929 for $\mathcal{F}_5$ to 1.6307 for $\mathcal{F}_7$. As a consequence, although initial conditions for a given frequency correspond to those of a propagating case, after several iterations the same frequency will likely be in a band gap. The meaning is that most of the initial conditions lead to an escaping [case c)] or a fully escaping [case d)] orbit on the Kohmoto's surface.

For $\sqrt{Q_L}\omega l_L = 0.15$ (Fig. 4/*b*)), a bounded orbit confined to the yellow portion of the surface $\{|\tilde{x}|, |\tilde{y}|, |\tilde{z}|\} \leq 2$ [case b)] is obtained, then at this frequency wave propagation is assured in structures generated by all first eight GM sequences. Conversely, for $\sqrt{Q_L}\omega l_L = 0.25$ (Fig. 4/*c*)) the orbit is an escaping one [case c)] for which the trace passes several times from a pass to a stop band and vice versa. Finally, for $\sqrt{Q_L}\omega l_L = 2.5$ (Fig. 4/*d*)) the orbit is fully escaping [case d)] for which the value of the trace x_i increases at each iteration and the orbit moves to lateral tails of the manifold ($\{|\tilde{x}|, |\tilde{y}|, |\tilde{z}|\} > 2$).

4.3 Linearisation of the maps about saddle points

Both non-periodic bounded trajectories, as those shown in Fig. 4/*b*) [case b)], and escaping trajectories, as those illustrated in Figs. 4/*c*) and /*d*) [cases c) and d)], can be

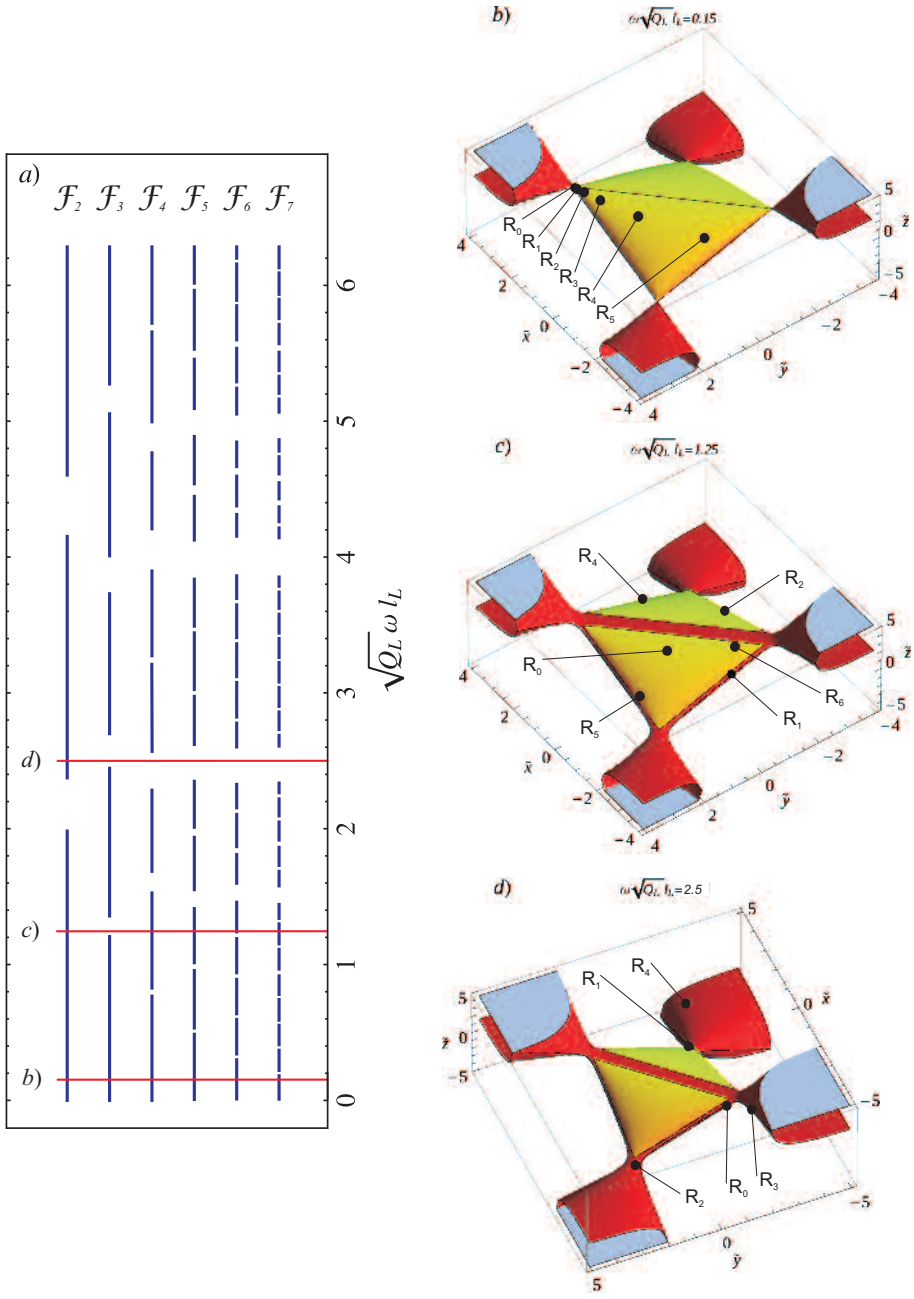

Figure 4: Traces of the transfer matrices corresponding to elementary cells $\mathcal{F}_2 - \mathcal{F}_7$ of GMSs mapped on the Kohmoto's manifold. In part *a*) the full stop/pass band layout is shown and the positions of the three selected frequencies *b*), *c*) and *d*) are identified by the three lines. In parts *b*), *c*) and *d*), the sets of points generated by iterating map (19) and defining the orbits for $\sqrt{Q_L}\omega l_L = 0.15, 1.25$ and 2.5 ($l_S = l_L/\sigma_g$ and $\rho_S = \rho_L/2$) are sketched on the corresponding surface. Points R_6 in *b*), R_3 in *c*) and R_5 in *d*) lie on a hidden part of the surface; R_6 in *d*) is on the lateral tails, out of the represented domain.

described as perturbations of the periodic orbit [case a)] on the Kohmoto's manifold at a

given ω. In order to introduce this important reference orbit, it is instrumental to refer to some relevant properties of the Kohmoto's surface.

Each manifold $I(\omega) = 0$ possesses six saddle points P_j $(j = 1, \ldots, 6)$ which are in antipodal positions in pairs. For GM and BM sequences, these points are connected to the periodic orbit [case a)] obtained, respectively, through the six-cycle transformations $\mathcal{T}_g^6$ and $\mathcal{T}_b^6$

$$\begin{aligned} P_1(0,0,a) &\xrightarrow{\mathcal{T}_{g,b}} P_2(-a,0,0) \xrightarrow{\mathcal{T}_{g,b}} P_3(0,-a,0) \\ &\xrightarrow{\mathcal{T}_{g,b}} P_4(0,0,-a) \xrightarrow{\mathcal{T}_{g,b}} P_5(a,0,0) \xrightarrow{\mathcal{T}_{g,b}} P_6(0,a,0) \xrightarrow{\mathcal{T}_{g,b}} P_1, \end{aligned} \tag{25}$$

where $a = \sqrt{4 + I(\omega)}$. $\mathcal{T}_g^6$ and $\mathcal{T}_b^6$ define a six-point periodic orbit for maps (19) and (21). Conversely, SM sequences are characterised by the four-cycle transformation $\mathcal{T}_s^4$

$$P_1(0,0,a) \xrightarrow{\mathcal{T}_s} P_3(0,-a,0) \xrightarrow{\mathcal{T}_s} P_4(0,0,-a) \xrightarrow{\mathcal{T}_s} P_6(0,a,0) \xrightarrow{\mathcal{T}_s} P_1, \tag{26}$$

which identifies a four-point periodic orbit for (20). It is important to highlight that P_j $(j = 1, ..., 6)$ are periodic points of maps (19) and (21) and fixed points of $\mathcal{T}_g^6$ and $\mathcal{T}_b^6$, whereas elements of the set $\{P_1, P_3, P_4, P_6\}$ are periodic points of (20) and fixed points of $\mathcal{T}_s^4$. Being periodic orbits, the starting point in both (25) and (26) can be any saddle point of the relevant transformation.

Even though periodic points depend uniquely on the property of the Kohmoto's surface, it may be interesting to note that for a real structure to follow the cyclic transformations (25) and (26) one of the following three conditions must be satisfied at a given ω:

$$\tilde{x}_0 = \tilde{y}_0 = 0, \quad \tilde{x}_0 = \tilde{z}_0 = 0, \quad \tilde{y}_0 = \tilde{z}_0 = 0. \tag{27}$$

This requirement can be observed only for a particular class of sequences, called here the class of *canonical sequences*, and at particular values of the frequency, denoted as *canonical frequencies*. For GMSs, conditions (27) imply that two of the expressions (15) vanish, and then, substituting the latter into (27), the following relationships are respectively derived

$$\frac{l_S}{l_L}\sqrt{\frac{Q_S}{Q_L}} = \frac{1+2j}{1+2k}, \quad \frac{l_S}{l_L}\sqrt{\frac{Q_S}{Q_L}} = \frac{1+2j}{2q}, \quad \frac{l_S}{l_L}\sqrt{\frac{Q_S}{Q_L}} = \frac{2q}{1+2k}, \quad \text{with } j,k,q \in \mathbb{N}. \tag{28}$$

By observing formulae (28), we can deduce that the main requirement to have a structure generated with a *canonical* sequence is that $(l_S/l_L)\sqrt{Q_S/Q_L} \in \mathbb{Q}$. Should this condition be satisfied, ordered pairs of natural numbers (j,k), (j,q) or (q,k) can be found which verify one of the relations (28). The corresponding *canonical* frequencies are then given by

$$\omega_{cj} = \frac{\pi}{2l_S\sqrt{Q_S}}(1+2j), \quad \omega_{ck} = \frac{\pi}{2l_L\sqrt{Q_L}}(1+2k), \quad \text{with } j,k \in \mathbb{N}. \tag{29}$$

More details regarding the properties of *canonical* sequences of GMSs are provided in Appendix A.

As just anticipated, we can study the escaping and non-periodic bounded trajectories of the traces on the Kohmoto's surface as perturbations of the periodic orbits defined by the cyclical transformations (25) and (26). Being a perturbative analysis, a reference saddle point should be selected which is the closest to the initial point R_i, and then, starting from this point, we can linearise the six- and four-cycle transformations (25) and (26). In what follow, we have assumed P_1 as the reference saddle point for the linearisation procedure, yielding (see, for example, Ott (1993))

$$R_{i+6} = \mathcal{T}_{g,b}^{6}(R_i) \;\Rightarrow\; \delta \boldsymbol{r}_{i+6} = \boldsymbol{A}_{g,b}\delta \boldsymbol{r}_i, \tag{30}$$

and

$$R_{i+4} = \mathcal{T}_{s}^{4}(R_i) \;\Rightarrow\; \delta \boldsymbol{r}_{i+4} = \boldsymbol{A}_{s}\delta \boldsymbol{r}_i, \tag{31}$$

respectively for $\mathcal{T}_{g,b}^{6}$ and $\mathcal{T}_{s}^{4}$. In (30)–(31),

$$\delta \boldsymbol{r}_i = R_i - P_1, \tag{32}$$

$$\begin{aligned} \boldsymbol{A}_{g,b} &= \boldsymbol{J}_{g,b}(P_6)\boldsymbol{J}_{g,b}(P_5)\boldsymbol{J}_{g,b}(P_4)\boldsymbol{J}_{g,b}(P_3)\boldsymbol{J}_{g,b}(P_2)\boldsymbol{J}_{g,b}(P_1), \\ \boldsymbol{A}_{s} &= \boldsymbol{J}_{s}(P_6)\boldsymbol{J}_{s}(P_4)\boldsymbol{J}_{s}(P_3)\boldsymbol{J}_{s}(P_1), \end{aligned} \tag{33}$$

where $\boldsymbol{J}_p(P_j)$ ($p = g, s, b$ in the remaining part of the paper) represents the Jacobian of maps (19)–(21) evaluated in the saddle point P_j using definition (22). The determinants of matrices $\boldsymbol{A}_p$ are unitary. For all three classes of structures, one eigenvalue is equal to one, i.e. $\kappa_p^0 = 1$, and the corresponding eigenvector is indicated with $\boldsymbol{w}_p^0$. For GMSs, the linearised transformation (30) has the additional pair of eigenvalues

$$\kappa_g^{\pm}(\omega) = \frac{1}{4}\Big(\sqrt{4 + (4 + I(\omega))^2} \pm (4 + I(\omega))\Big)^2, \tag{34}$$

whereas for BM sequences the same pair is

$$\kappa_b^{\pm}(\omega) = \frac{1}{4}\Big(\sqrt{4 + (4 + I(\omega))^2(9 + 4I(\omega))^2} \pm (4 + I(\omega))(9 + 4I(\omega))\Big)^2. \tag{35}$$

Similarly, the linearised transformation (31) possesses the eigenvalues

$$\kappa_s^{\pm}(\omega) = \Big(\sqrt{(3 + I(\omega))^2 - 1} \pm (3 + I(\omega))\Big)^2. \tag{36}$$

For all pairs (34)–(36), $\kappa_p^{+}(\omega) = 1/\kappa_p^{-}(\omega)$. They are associated with the eigenvectors $\boldsymbol{w}_p^{\pm}$ defined as

$$\boldsymbol{A}_p \boldsymbol{w}_p^{\pm} = \kappa_p^{\pm} \boldsymbol{w}_p^{\pm}, \tag{37}$$

where the dependence of eigenvalues on the circular frequency has been dropped.

$\boldsymbol{A}_p$ are partitioned matrices[2] with a symmetric 2×2 block such that $\boldsymbol{w}_p^0$ is orthogonal to the Kohmoto's surface at the point P_j, while the other two eigenvectors are in turn orthogonal and span the tangent plane to the manifold, say $\pi_{p,j}$. The set $\{\boldsymbol{w}_p^+, \boldsymbol{w}_p^-, \boldsymbol{w}_p^0\}$ defines a basis of the space where $\delta\boldsymbol{r}_i$ is represented, and then we can express $\delta\boldsymbol{r}_i$ for all the three maps as

$$\delta\boldsymbol{r}_i = C_p^+\boldsymbol{w}_p^+ + C_p^-\boldsymbol{w}_p^- + C_p^0\boldsymbol{w}_p^0. \tag{38}$$

Applying the linearised transformations (30) and (31) to the vector (38), and recalling the definition of eigenvector, we obtain

$$\delta\boldsymbol{r}_{i+6} = \boldsymbol{A}_{g,b}\delta\boldsymbol{r}_i = C_{g,b}^+\kappa_{g,b}^+\boldsymbol{w}_{g,b}^+ + C_{g,b}^-\kappa_{g,b}^-\boldsymbol{w}_{g,b}^- + C_{g,b}^0\boldsymbol{w}_{g,b}^0, \tag{39}$$

and

$$\delta\boldsymbol{r}_{i+4} = \boldsymbol{A}_s\delta\boldsymbol{r}_i = C_s^+\kappa_s^+\boldsymbol{w}_s^+ + C_s^-\kappa_s^-\boldsymbol{w}_s^- + C_s^0\boldsymbol{w}_s^0. \tag{40}$$

By inspection of expressions (34)–(36), it can be verified that for any value of the frequency, $\kappa_p^+ \gg 1 \gg \kappa_p^-$ (see also plots in Appendix B computed for a GM rod), and then if we apply k times the linearized maps (39) and (40), the outcome is

$$\delta\boldsymbol{r}_{i+6k} = C_{g,b}^+(\kappa_{g,b}^+)^k\boldsymbol{w}_{g,b}^+ + C_{g,b}^-(\kappa_{g,b}^-)^k\boldsymbol{w}_{g,b}^- + C_{g,b}^0\boldsymbol{w}_{g,b}^0 \approx (\kappa_{g,b}^+)^k C_{g,b}^+\boldsymbol{w}_{g,b}^+, \tag{41}$$

and

$$\delta\boldsymbol{r}_{i+4k} = C_s^+(\kappa_s^+)^k\boldsymbol{w}_s^+ + C_s^-(\kappa_s^-)^k\boldsymbol{w}_s^- + C_s^0\boldsymbol{w}_s^0 \approx (\kappa_s^+)^k C_s^+\boldsymbol{w}_s^+, \tag{42}$$

for the two types of maps. From eqs. (41) and (42) we can deduce that, every six iterations for GMSs and BMSs and four iterations for SMSs, the evolution of $\delta\boldsymbol{r}_i$ can be approximated counting only on the component of $\delta\boldsymbol{r}_i$ lying respectively along the eigenvectors $\boldsymbol{w}_g^+$, $\boldsymbol{w}_b^+$ and $\boldsymbol{w}_s^+$, which define the so-called unstable eigendirections (see, for example, Arnold (1989)). Therefore, (41) and (42) are approximated by

$$\delta\boldsymbol{r}_{i+6k} \approx (\kappa_{g,b}^+)^k\delta\hat{\boldsymbol{r}}_i \quad \text{and} \quad \delta\boldsymbol{r}_{i+4k} \approx (\kappa_s^+)^k\delta\hat{\boldsymbol{r}}_i, \tag{43}$$

where $\delta\hat{\boldsymbol{r}}_i = C_{g,b}^+\boldsymbol{w}_{g,b}^+$ in the former and $\delta\hat{\boldsymbol{r}}_i = C_s^+\boldsymbol{w}_s^+$ in the latter. It is worth recalling that $\delta\hat{\boldsymbol{r}}_i$ and the estimations of $\delta\boldsymbol{r}_{i+6k}$ and $\delta\boldsymbol{r}_{i+4k}$ provided by (43) all lie on the tangent plane $\pi_{p,j}$.

In line with the principles of renormalization theory, eqs. (43) provide the approximate evolution of the position of R_i from the fixed point P_1 in the case in which the former is in the neighbourhood of the latter. This approach illustrates the scaling properties of non-periodic bounded orbits about the fixed points of the transformations that is governed by the eigenvalue κ_p^+ of the relevant map. It is important to observe that,

[2]with the assumption of P_1 as a saddle point, for GM rods,

$$\boldsymbol{A}_g = \begin{bmatrix} I(\omega)^2+7I(\omega)+13 & (I(\omega)+4)^{3/2} & 0 \\ (I(\omega)+4)^{3/2} & I(\omega)+5 & 0 \\ 0 & 0 & 1 \end{bmatrix}.$$

i) if we study the evolution of $\delta \boldsymbol{r}_i$ through the linearised analysis, the norm $||\delta \boldsymbol{r}_{i+6k}||$ increases at each iteration for any set of initial conditions; then, at each iteration, the distance between the transformed point and the fixed point P_j increases, and then the orbits defined by the approximated maps are always open and never periodic, as most of the orbits determined by the exact nonlinear transformations (19)–(20) and illustrated by the examples reported in Fig. 4;

ii) taking into account cycles (25) and (26), it is clear that each application of the generic operator $\boldsymbol{J}(P_j)$ in (33) projects the current vector $\delta \boldsymbol{r}_h$ to the neighborhood of the subsequent point of the cycle. As an example, $\boldsymbol{J}_g(P_3)\boldsymbol{J}_g(P_2)\boldsymbol{J}_g(P_1)\delta \boldsymbol{r}_1$ is a vector that must be interpreted with reference to point P_4.

5 Scaling, self-similarity of the spectrum and ultrawide band gaps

Scaling and self-similarity of the stop/pass band layout will be analysed in this section for GM and SM rods for the same parameters adopted in Figs. 2 and 3 in the range of frequencies $0 \leq \sqrt{Q_L}\omega l_L \leq 2\pi$. The outcome is reported in Figs. 5 and 7, respectively, where, similarly to Fig. 4, blue lines (white gaps) denote pass (stop) bands.

For GMSs, the analysed sequences in Fig. 5 are $\mathcal{F}_2$ to $\mathcal{F}_8$. Here, we observe that the set of stop/pass band diagrams exhibit a self-similar pattern as the generation index i increases. At each iteration, each pass band splits into a number of shorter pass bands in the subsequent row that follow the recursive rule of Fibonacci numbers n_i, i.e. $1, 1, 2, 3, 5, \cdots$. Moreover, the number of pass bands for a generic sequence $\mathcal{F}_i$ is equal to n_{i+1}, and the number of band gaps equals $n_{i+1} - 1$.

The graph is endowed with different properties.

1) *Ultrawide* band gaps: the chart in Fig. $5/a$) clearly displays four intervals of frequencies that are in a band gap for all cells generated by $\mathcal{F}_{j+4}$ ($j = 0, 1, 2, \dots$). These intervals are definitely wider than other band gaps, and then further in the text we will call them *ultrawide* band gaps. They are associated with fully escaping orbits [case d)]. Section 6 will be devoted to their analysis.

2) 'Local' scaling of the spectrum about some frequencies: outside the ranges of frequencies affected by *ultrawide* band gaps, parts of the diagram for a given sequence scale down at increasing index i.

3) Scaling of large portions of the dynamic spectrum: the layout in a relatively large frequency range can be identified downscaled in the diagram obtained for a higher index i.

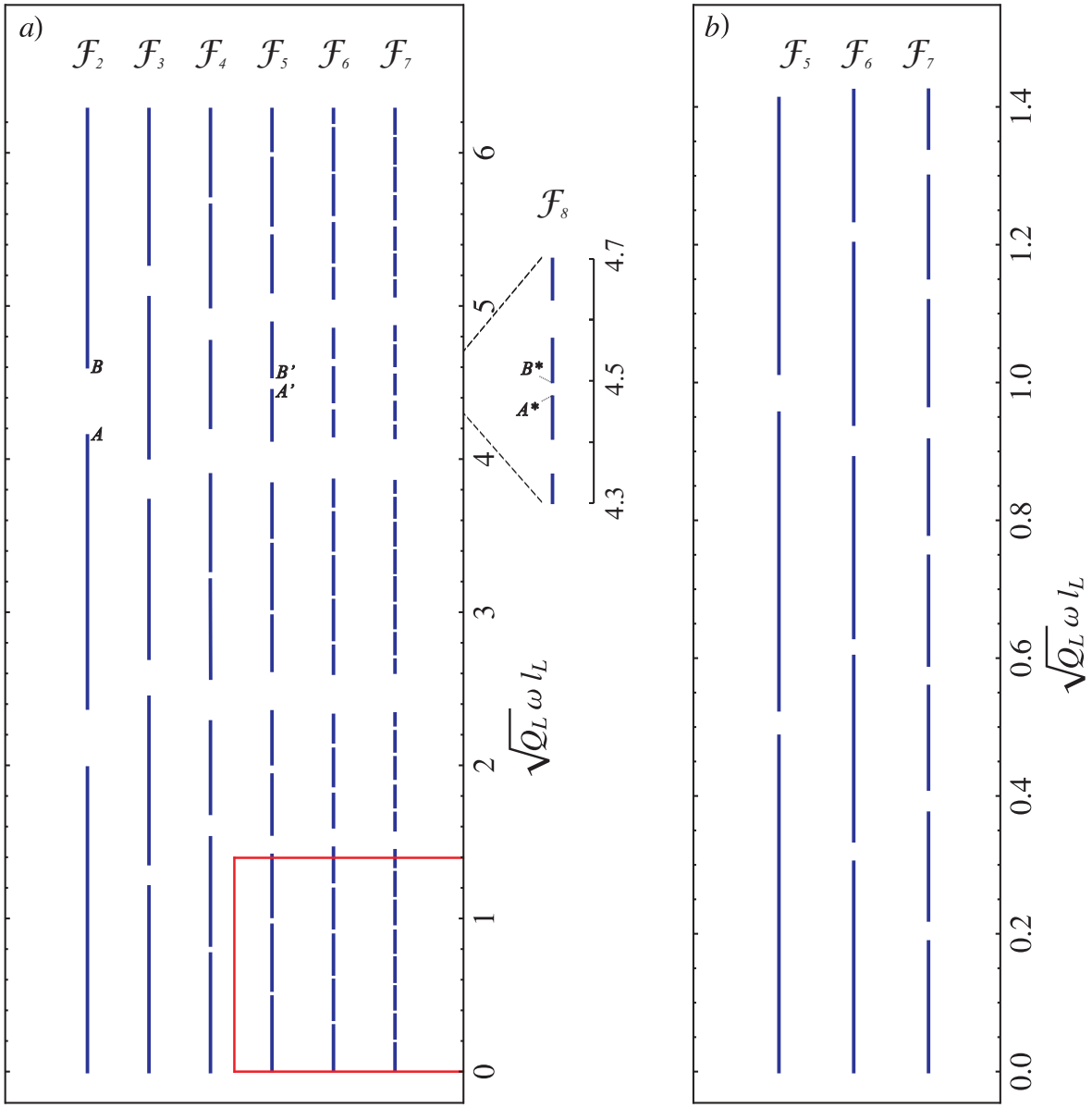

Figure 5: Stop/pass band diagram for rods generated by cells $\mathcal{F}_2$ to $\mathcal{F}_8$ of the GM sequence assuming $l_S = l_L/\sigma_g$ and $\rho_S = \rho_L/2$. The band gap in the diagram $\mathcal{F}_8$ detailed in *a*) is between $\sqrt{Q_L}\omega_{A^*} l_L = 4.477$ and $\sqrt{Q_L}\omega_{B^*} l_L = 4.497$. The close up view *b*) illustrates the diagram associated with the cells $\mathcal{F}_5$, $\mathcal{F}_6$ and $\mathcal{F}_7$ in the domain rescaled using the scaling factor $\bar{\lambda}_g$, that is the average value of $\lambda_g = \sqrt{\kappa_g}$ evaluated upon the range $0 \leq \sqrt{Q_L}\omega l_L \leq 2\pi$.

5.1 'Local' scaling of the spectrum about some frequencies

This type of scaling, that has a 'local' nature, is illustrated through an example involving a narrow stop band for which it is shown the role of the eigenvalue κ_p^+. A similar procedure can be applied to other stop bands located outside *ultrawide* band-gap regions. Consider

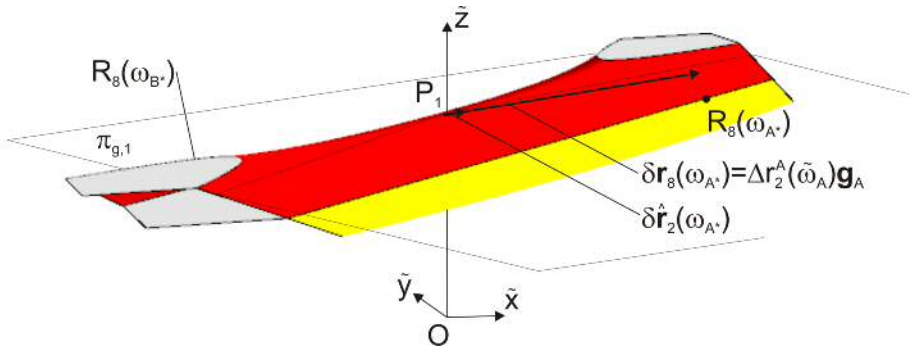

Figure 6: Kohmoto's surface for $\sqrt{Q_L}\omega l_L = 4.487$ in the neighborhood of the saddle point P_1 for the GM rods considered in Fig. 5. Point $R_8(\omega_{B^*})$ is not visible. The tangent plane $\pi_{g,1}$ has equation $\tilde{z} = +a$.

the stop band $\{\omega_{A^*} - \omega_{B^*}\}$ in the diagram for $\mathcal{F}_8$ centred at $\sqrt{Q_L}\omega l_L = 4.487$ in Fig. 5/a)[3]. Points $R_8(\omega_{A^*})$ and $R_8(\omega_{B^*})$ are therefore on the boundary of a yellow region of the Kohmoto's surface for $\sqrt{Q_L}\omega l_L = 4.487$, in this case in the neighbourhood of the saddle point P_1 (see Fig. 6). The positions of the two points with respect to P_1 can be approximated by two vectors, respectively $\delta\boldsymbol{r}_8(\omega_{A^*})$ and $\delta\boldsymbol{r}_8(\omega_{B^*})$, on the tangent plane $\pi_{g,1}$ of P_1 whose equation is $\tilde{z} = +a$. Then, eq. $(43)_1$ can be invoked backwards with $k = 1$ to yield, respectively,

$$\delta\hat{\boldsymbol{r}}_2(\omega_{A^*}) = \frac{\delta\boldsymbol{r}_8(\omega_{A^*})}{\kappa_g} \quad \text{and} \quad \delta\hat{\boldsymbol{r}}_2(\omega_{B^*}) = \frac{\delta\boldsymbol{r}_8(\omega_{B^*})}{\kappa_g}, \tag{44}$$

where κ_g is the eigenvalue κ_g^+ evaluated at $\sqrt{Q_L}\omega l_L = 4.487$. The two new vectors are on the same tangent plane $\pi_{g,1}$, but they are much shorter than the parent vectors $\delta\boldsymbol{r}_8(\omega_{A^*})$ and $\delta\boldsymbol{r}_8(\omega_{B^*})$. Their vertical projections to the surface identify approximated points $R_2(\omega_{A^*})$ and $R_2(\omega_{B^*})$, respectively, whose coordinates $\tilde{z}_2(\omega_{A^*})$ and $\tilde{z}_2(\omega_{B^*})$ are greater then 2, therefore the two frequencies are within a band gap for $\mathcal{F}_2$ (Fig. 6). Now, let us write $\delta\hat{\boldsymbol{r}}_2(\omega_{A^*})$ as

$$\delta\hat{\boldsymbol{r}}_2(\omega_{A^*}) = \Delta r_2^A(\omega)_{|\omega=\omega_{A^*}}\boldsymbol{g}_A, \tag{45}$$

where $\boldsymbol{g}_A$ is a unit vector and assume that the function $\Delta r_2^A(\omega)$ can be expanded in Taylor series about ω_{P_1} retaining only the linear term, namely

$$\Delta r_2^A(\omega) \approx D(\omega - \omega_{P_1}) \quad (D < 0). \tag{46}$$

The approximate frequency $\tilde{\omega}_A$ at the edge of a band gap for the sequence $\mathcal{F}_2$ is such that $\Delta r_2^A(\tilde{\omega}_A)$ matches the norm of vector $\delta\boldsymbol{r}_8(\omega_{A^*})$, namely

$$\Delta r_2^A(\tilde{\omega}_A) = ||\delta\boldsymbol{r}_8(\omega_{A^*})||. \tag{47}$$

[3]We assume that in this range the Kohmoto's invariant is constant, so we refer in this subsection to the manifold for $\sqrt{Q_L}\omega l_L = 4.487$.

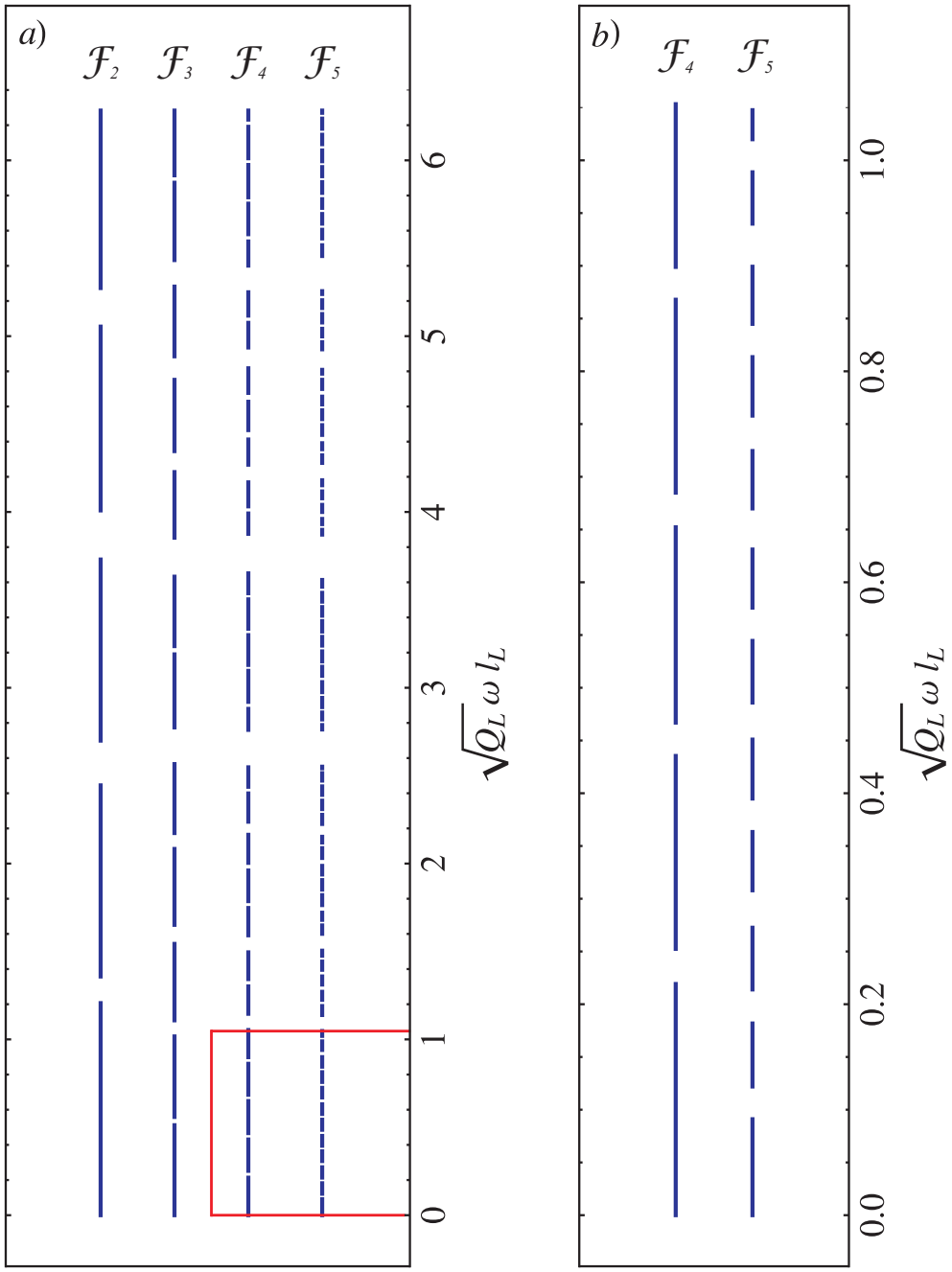

Figure 7: Stop/pass band diagram for rods generated by cells $\mathcal{F}_2$ to $\mathcal{F}_5$ of the Fibonacci SM sequence assuming $l_S = l_L/\sigma_g$ and $\rho_S = \rho_L/2$. The close up view b) illustrates the diagram associated with the cells $\mathcal{F}_4$ and $\mathcal{F}_5$ in the domain rescaled using the scaling factor $\bar{\lambda}_s$, that is the average value of $\lambda_s = \sqrt{\kappa_s}$ evaluated upon the range $0 \leq \sqrt{Q_L}\omega l_L \leq 2\pi$.

The use of $(44)_1$ and (46) yields

$$D(\tilde{\omega}_A - \omega_{P_1}) = \kappa_g D(\omega_{A^*} - \omega_{P_1}), \tag{48}$$

therefore, the following final result can be recorded

$$\omega_{P_1} - \omega_{A^*} = \frac{\omega_{P_1} - \tilde{\omega}_A}{\kappa_g}. \tag{49}$$

A similar procedure can be followed for $\delta\hat{\boldsymbol{r}}_2(\omega_{B^*})$, obtaining $\omega_{B^*} - \omega_{P_1} = (\tilde{\omega}_B - \omega_{P_1})/\kappa_g$, so that the following scaling law can be established

$$\omega_{B^*} - \omega_{A^*} = \frac{\tilde{\omega}_B - \tilde{\omega}_A}{\kappa_g}. \tag{50}$$

The band gap $\{\tilde{\omega}_A - \tilde{\omega}_B\}$ approximates the real one ($\{\omega_A - \omega_B\}$) in the $\mathcal{F}_2$ diagram, depicted in Fig. $5/a$). The quality of the scaling described by eq. (50) is remarkably good: for the selected example, $\kappa_g = 21.37$, while the ratio $(\omega_B - \omega_A)/(\omega_{B^*} - \omega_{A^*})$ is equal to 22.43.

With the proposed example, we have shown how the 'local' scaling occurring between parts of the diagrams of $\mathcal{F}_i$ and $\mathcal{F}_{i+6}$ (in this case $i = 2$) is governed by $(43)_1$, coherently with the linearisation of the six-cycle transformation $\mathcal{T}_g^6$. The same method can be applied to parts of the spectra computed for the other two types of sequences: in particular, for SMSs, if relevant, the scaling applies between $\mathcal{F}_i$ and $\mathcal{F}_{i+4}$.

With a similar approach, but without the full support of the theory leading to eq. (43), we can give an explanation of the scaling between, again, $\{\omega_{A^*} - \omega_{B^*}\}$ and the band gap $\{\omega_{A'} - \omega_{B'}\}$ in the diagram for $\mathcal{F}_5$, which contains the dimensionless frequency $\sqrt{Q_L}\omega l_L = 4.487$. In this case, we are able to establish a link between $\mathcal{F}_i$ and $\mathcal{F}_{i+3}$.

Let us define the matrix governing the three-step linearised map, corresponding to the second half of the six-step transformation (33) as

$$\boldsymbol{B}_{g,b} = \boldsymbol{J}_{g,b}(P_6)\boldsymbol{J}_{g,b}(P_5)\boldsymbol{J}_{g,b}(P_4)$$

(an analogous map can be defined for SMSs), and in our example, compute the approximate vectors

$$\delta\hat{\boldsymbol{r}}_5(\omega_{A^*}) = \boldsymbol{B}_g^{-1}\delta\boldsymbol{r}_8(\omega_{A^*}) \quad \text{and} \quad \delta\hat{\boldsymbol{r}}_5(\omega_{B^*}) = \boldsymbol{B}_g^{-1}\delta\boldsymbol{r}_8(\omega_{B^*}). \tag{51}$$

According to the observation ii) made at the end of subsection 4.3, the two vectors describe points that must be considered in relation to saddle point P_4. Their vertical projections to the Kohmoto's surface in the neighborhood of P_4 identify points that are in a band gap. We can repeat a procedure similar to that developed for $\delta\hat{\boldsymbol{r}}_2(\omega_{A^*})$ and $\delta\hat{\boldsymbol{r}}_2(\omega_{B^*})$ (based on eqs. (45) and (46)) to obtain

$$\omega_{B^*} - \omega_{A^*} = \frac{\tilde{\omega}_{B'} - \tilde{\omega}_{A'}}{\lambda_g}, \tag{52}$$

where $\tilde{\omega}_{A'}$ and $\tilde{\omega}_{B'}$ are the two approximate frequencies at the edge of the band gap for the sequence $\mathcal{F}_5$. In our example, the parameter λ_g turns out to be 4.62, while for the

actual gap $\{\omega_{A'} - \omega_{B'}\}$, the ratio $(\omega_{B'} - \omega_{A'})/(\omega_{B^*} - \omega_{A^*})$ is equal to 4.63, so the match is again extremely good.

We note that with very good agreement, $\lambda_g \simeq \sqrt{\kappa_g}$. Actually, this is not surprising as λ_g governs the scaling of the initial band gap of the example after the application of three of the six multiplicative steps of application (33).

5.2 Scaling of large portions of the dynamic spectrum

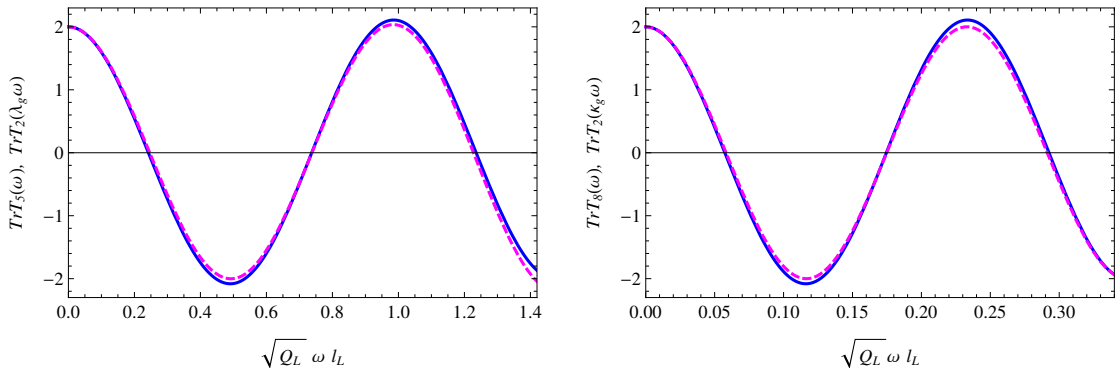

Figure 8: Study of the downscaling of the dynamic spectra for GM rods with $l_S = l_L/\sigma_g$ and $\rho_S = \rho_L/2$. On the left, plot of $x_5(\omega)$ (magenta dashed line) and $x_2(\bar{\lambda}_g\omega)$ (blue solid line). On the right, functions $x_8(\omega)$ (magenta dashed line) and $x_2(\bar{\kappa}_g\omega)$ (blue solid line) are displayed.

A different type of scaling is introduced now and involves a large portion of the dynamic spectrum. In Figs. $5/a$) and $7/a$), the red contours highlight the downscaling of the whole frequency range $0 \leq \sqrt{Q_L}\omega l_L \leq 2\pi$. This portion of the spectrum is zoomed in in parts b) of the two figures. In the re-scaled domain of Fig. $5/b$), the stop/pass band layout of $\mathcal{F}_5$ is very similar to that of $\mathcal{F}_2$ in the wider interval. A similar behaviour is identified in Fig. $7/b$) for the diagrams for $\mathcal{F}_4$ and $\mathcal{F}_5$ with respect to those for $\mathcal{F}_2$ and $\mathcal{F}_3$, respectively.

The downscaling is related to the property

$$x_{i+3}(\omega) \approx x_i(\bar{\lambda}_{g,b}\,\omega) \tag{53}$$

for GMSs and BMSs, and

$$x_{i+2}(\omega) \approx x_i(\bar{\lambda}_s\,\omega) \tag{54}$$

for SMSs, where $\bar{\lambda}_p$ is the average value of the parameter λ_p introduced in the previous subsection[4] upon a given frequency range. The choice of this range is not unique as, alternatively, we can see the wider domain $0 \leq \sqrt{Q_L}\omega l_L \leq 2\pi$ as the result of an upscaling of the frequency interval corresponding to the red contours[5]. Whatever the choice,

[4]actually, only λ_g was defined, but both λ_b and λ_s can be introduced in a similar way.

[5]in the range $0 \leq \sqrt{Q_L}\omega l_L \leq 2\pi$, $\bar{\lambda}_g = \overline{\sqrt{\kappa_g}} = 4.37$, whereas for the red contour domain, $0 \leq \sqrt{Q_L}\omega l_L \leq 1.4$, $\bar{\lambda}_g = \overline{\sqrt{\kappa_g}} = 4.29$.

however, the variation in the parameter $\bar{\lambda}_p$ is very limited. The panel on the left of Fig. 8 shows numerically the correspondence (53) for $i = 2$ computed for $\bar{\lambda}_g = 4.40$ (the magenta dashed line represents the function $x_5(\omega)$, while the solid blue line is the graph of $x_2(\bar{\lambda}_g\omega)$). This value has been selected to show the almost perfect match between the stationary points of the two functions; nevertheless, by comparing the diagram for $\mathcal{F}_2$ in part *a*) to that for $\mathcal{F}_5$ in part *b*) of Fig. 5, we note that the two band gaps are not perfectly aligned.

On the panel on the right, the property $x_{i+6}(\omega) \approx x_i(\bar{\kappa}_g\,\omega)$ is demonstrated on the scaled domain $0 \leq \sqrt{Q_L}\omega l_L \leq 0.33$ obtained by adopting $\bar{\kappa}_g = 18.90$, confirming that the type of scaling addressed in this subsection is also valid when a complete six-step cycle is considered.

6 Ultrawide band gaps

We now propose a heuristic strategy to predict the position of *ultrawide* band gaps within the spectrum studying the local maxima and minima of a properly defined approximant function. Let us introduce the function $H(\omega) = x_2(\omega)x_3(\omega)$ and recall the recursive relations (14), (16) and (17), valid for GM, SM and BM rods, respectively. For the GM case, consider now a frequency ω^* associated with a local maximum or minimum of the function $H(\omega)$ such that $|H(\omega^*)| \gg 2$. At the order $i = 4$, the relation (14) can be approximated as

$$x_4(\omega^*) = x_2(\omega^*)x_3(\omega^*) - x_1(\omega^*) \approx x_2(\omega^*)x_3(\omega^*) = H(\omega^*), \tag{55}$$

where we have used the following property of the trace corresponding to the elementary cell of the sequence: $|x_1(\omega^*)| \leq 2$ (see eq. $(15)_2$). It is important to note that as $|H(\omega^*)| \gg 2$, the assumption of expression (55) implies automatically that ω^* is in a band gap for the cell $\mathcal{F}_4$. Moreover, using (55) as a starting point and assuming that $x_{i+5} \approx x_{i+4}x_{i+3}$, traces of the transfer matrices associated with orders higher than 4 can be approximated by

$$x_{j+5}(\omega^*) \approx \frac{(H(\omega^*))^{n_{j+2}}}{(x_2(\omega^*))^{n_j}}, \quad \text{with } j \geq 0. \tag{56}$$

We focus now on the denominator of eq. (56). Due to the properties of expression $(15)_3$, $0 \leq |x_2(\omega)| \leq x_2^{max}$, with $x_2^{max} \gtrsim 2$. As a consequence, since $|H(\omega^*)| \gg 2$ and $n_{j+2} > n_j$, $x_2^{max} \leq |H(\omega^*)|$, and then

$$2 < \left| \frac{(H(\omega^*))^{n_{j+2}}}{(x_2(\omega^*))^{n_j}} \right| < +\infty, \quad \text{with } j \geq 0. \tag{57}$$

From relation (57), assuming for $\omega = \omega^*$ the approximated expressions (55) and (56), we obtain

$$2 < |x_{i+5}(\omega^*)| < +\infty, \quad \text{with } j \geq 0. \tag{58}$$

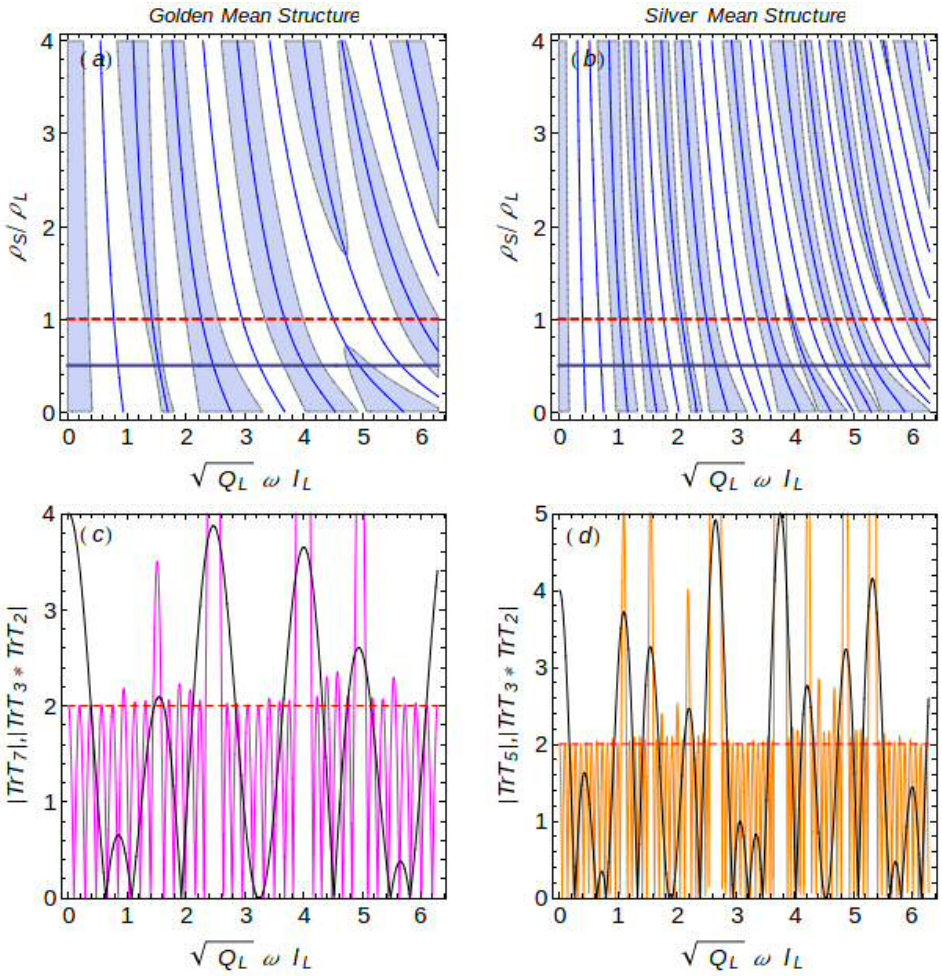

Figure 9: *Ultrawide* band gaps for GM (left column) and SM (right column) structures for $l_L/l_S = \sigma_g$. In parts *a*) and *b*) sector plots of the function $|H(\omega)|$ are shown. The regions where $|H(\omega)| \geq 2$ are highlighted in light blue, whereas the white regions correspond to $|H(\omega)| < 2$, and the thin blue curves denote the local maxima. The dark blue straight line indicates the value $\rho_S/\rho_L = 1/2$ assumed in the evaluation of $|\mathrm{tr}\,\boldsymbol{T}_7|$ (magenta line) and $|\mathrm{tr}\,\boldsymbol{T}_5|$ (orange line) plotted in parts *c*) and *d*). Ultra-wide band gaps are localized in proximity of the maxima of $|H(\omega)|$ (black lines) for values greater than 2.

Recalling that for a cell $\mathcal{F}_i$ a frequency is in a band gap if $|x_i(\omega)| > 2$ (see eq. (13)), eq. (58) implies that for $\omega = \omega^*$ all the GMSs whose elementary cells are generated by $\mathcal{F}_{j+5}$ ($j \geq 0$) are in a stop band, and then ω^* is associated with one of the *ultrawide* band gaps identified in Figs. 5/*a*) and 7/*a*). Similar results can be obtained for both BMSs and SMSs by approximating relations $(16)_2$ and $(17)_2$ at the order $i = 4$ for $\omega = \omega^*$ as follows: $t_4(\omega^*) \approx x_2(\omega^*)x_3(\omega^*) = H(\omega^*)$. Consequently, we can state that for all *precious* mean structures, if $H(\omega)$ possesses a local stationary point $\omega = \omega^*$ such that $|H(\omega^*)| \gg 2$, this value of the frequency lies in a *ultrawide* band gap. Therefore, the position of these large stop bands inside the spectrum can be predicted studying the local maxima of $|H(\omega)|$.

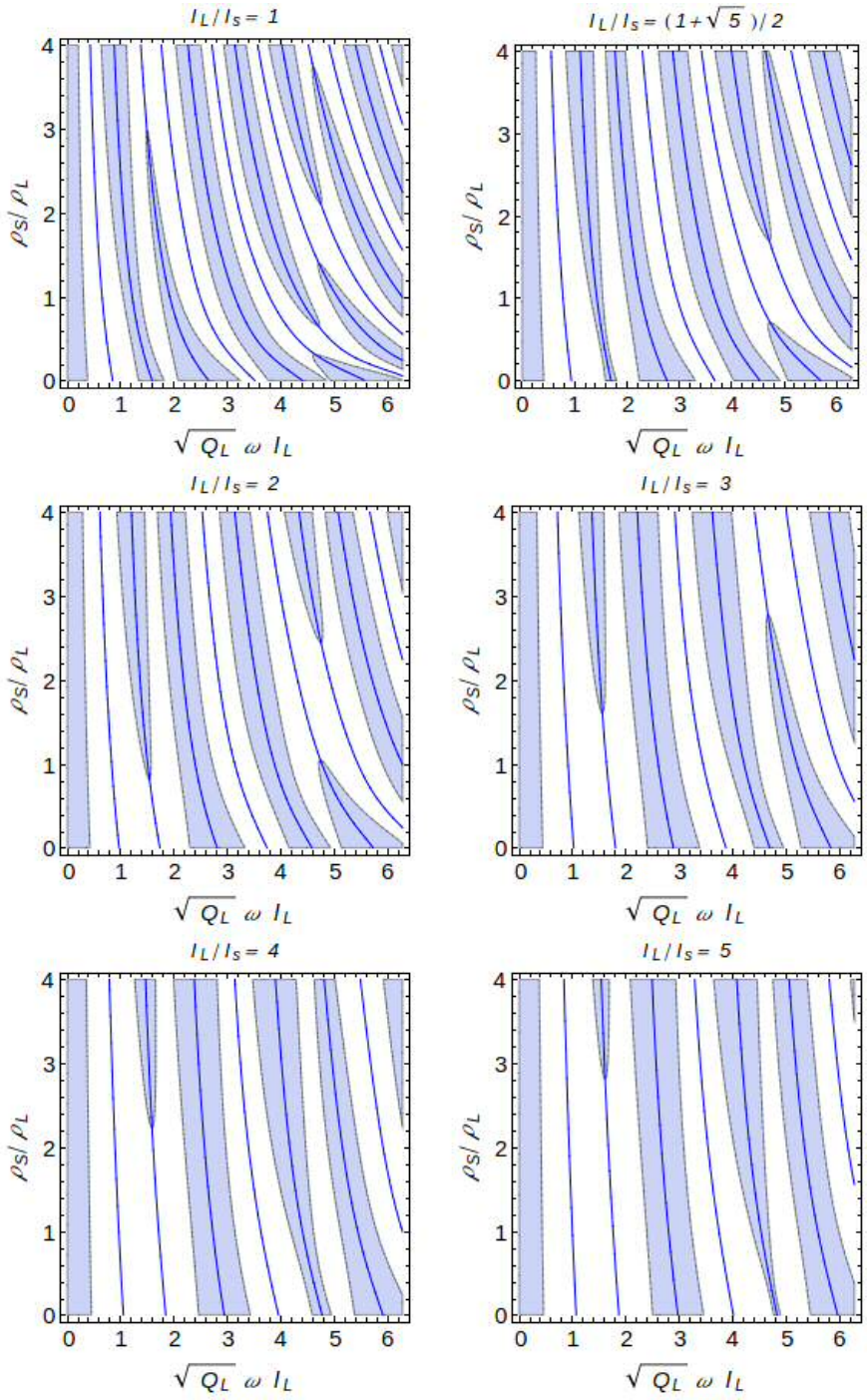

Figure 10: Sector plots of the quantity $|H(\omega)|$ corresponding to GMSs for $\rho_S = \rho_L/2$, reported for several values of the ratio l_L/l_S. The regions where $|H(\omega)| \geq 2$, that give an estimate of the position of *ultrawide* band gaps, are highlighted in light blue, and the thin blue lines correspond to local maxima of the same function.

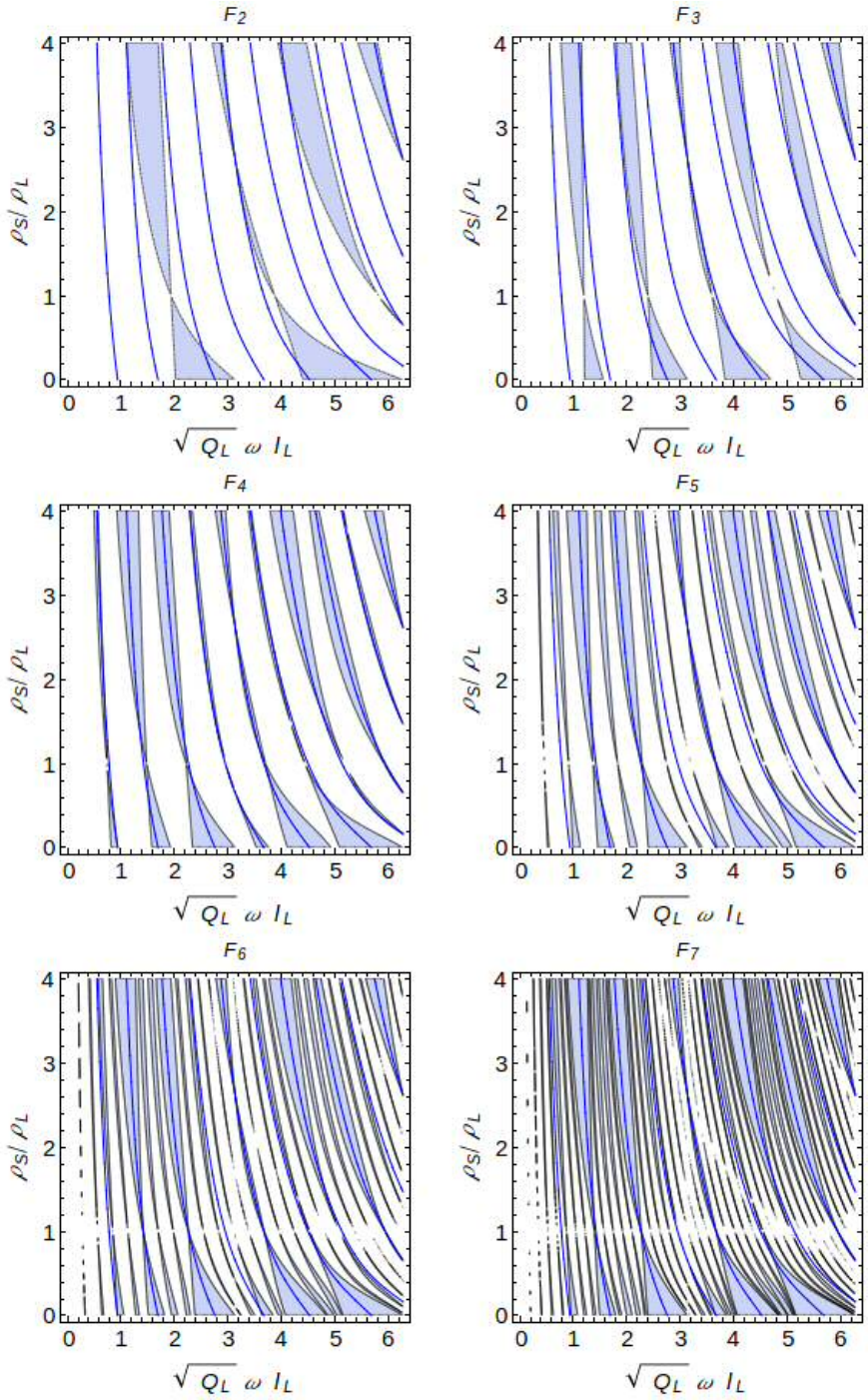

Figure 11: Sector plots of $|\mathrm{tr}\,\boldsymbol{T}_i|$ $(i = 2, \ldots, 7)$ for GMSs evaluated assuming $l_S = l_L/\sigma_g$ and $\rho_S = \rho_L/2$. The band-gap regions ($|\mathrm{tr}\,\boldsymbol{T}_i| \geq 2$) are highlighted in light blue. The thin blue lines denote the local maxima of $|H(\omega)|$.

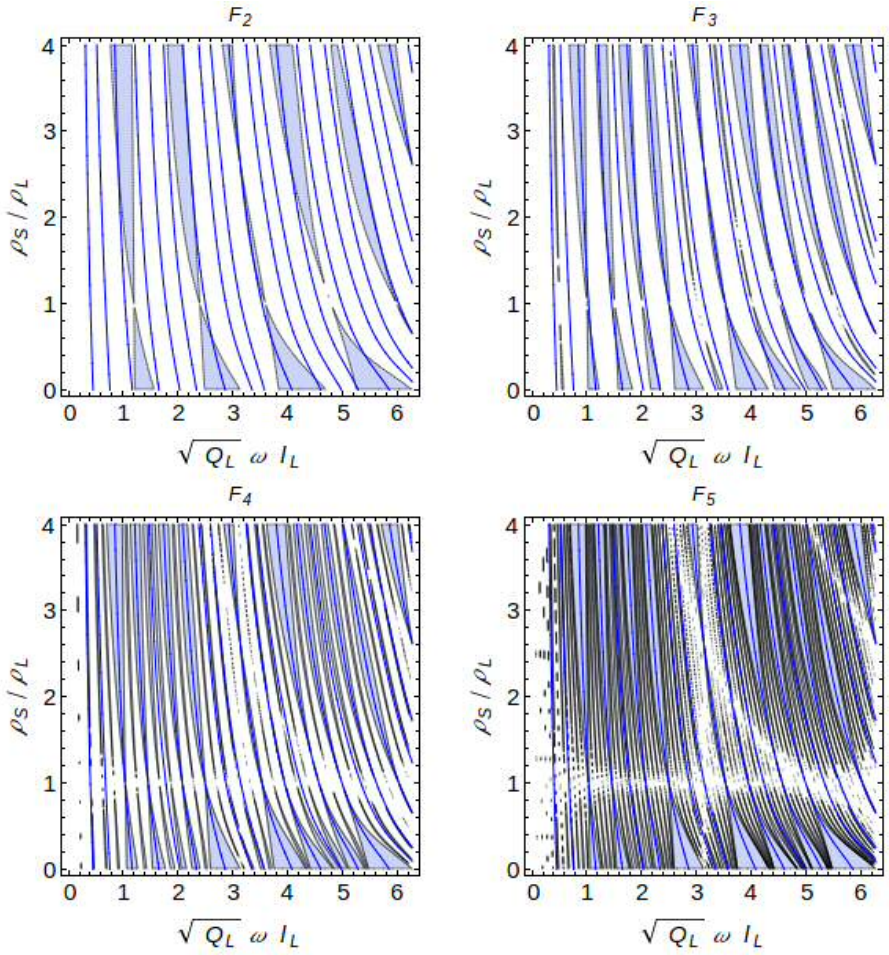

Figure 12: Sector plots of $|\mathrm{tr}\,\boldsymbol{T}_i|$ $(i = 2, \ldots, 5)$ for SMSs evaluated assuming $l_S = l_L/\sigma_g$ and $\rho_S = \rho_L/2$. The band-gap regions ($|\mathrm{tr}\,\boldsymbol{T}_i| \geq 2$) are highlighted in light blue. The thin blue lines denote the local maxima of $|H(\omega)|$.

The validity of the proposed criterion is demonstrated by the plots reported in Fig. 9. The sector plots of the function $|H(\omega)|$ are shown in Fig. $9/a$) for GMSs and Fig. $9/b$) for SMSs ($l_L/l_S = \sigma_g$) in which normalised frequency $\sqrt{Q_L}\omega l_L$ and density ratio ρ_S/ρ_L are reported on the horizontal and vertical axes, respectively. The regions where $|H(\omega)| \geq 2$ are highlighted in light blue, whereas the white regions correspond to $|H(\omega)| < 2$; the thin blue lines denote the local maxima of $|H(\omega)|$. The thick, dark blue horizontal lines reported for $\rho_S/\rho_L = 1/2$ indicate the value for the density ratio assumed in the evaluation of the curves reported in Figs. $9/c$) and $9/d$). In Fig. $9/c$), the quantity $|x_7|$ for the GMSs is plotted as a function of the normalised frequency (magenta line) together with $|H(\omega)|$ (black line). We note that the *ultrawide* band gaps of $\mathcal{F}_7$, revealed by $|x_7| \gg 2$, correspond to the maxima of $|H(\omega)|$ for which $|H(\omega)| > 2$. These maxima can be easily identified in Fig. $9/a$) at the intersection points between the horizontal thick blue line

and the thin curved lines crossing the light-blue regions, which are indeed associated with $|H(\omega)| > 2$. The function $|x_5|$ for SMSs displays a similar behaviour (orange line in Fig. 9/*d*)) where $|H(\omega)|$ is again sketched with a solid black curve. Therefore, the light blue regions in parts *a*) and *b*) provide a good estimate of the position of *ultrawide* band gaps for different density contrasts at the selected ratio l_L/l_S.

Sector plots of $|H(\omega)|$ are shown in Fig. 10 for different values of the ratio l_L/l_S. We observe that as this parameter increases, the number of regions where $|H(\omega)| \geq 2$, highlighted in light blue, decreases. This means that when $l_L \gg l_S$, the number of these wide stop bands decreases in the same frequency range, while their density increases when the two lengths are comparable.

Sector plots reported in Fig. 11 illustrate the whole stop/pass band arrangement for GMSs generated according to sequences from $\mathcal{F}_2$ to $\mathcal{F}_7$ assuming $l_L/l_S = \sigma_g$. The band-gap regions, where $|x_i| \geq 2$, are highlighted in light blue, whereas pass bands are reported in white. As in the previous figures, the thin blue lines denote the local maxima of $|H(\omega)|$. Differently from Fig. 9/*a*), in Fig. 11 all band gaps are represented, including both *ultrawide* and standard band gaps for which scaling applies. On the one hand, by observing the sector plots associated with the different sequences, we note that only for $\mathcal{F}_2$ and $\mathcal{F}_3$ a few large band gap areas appear, and then from $\mathcal{F}_4$ on these are localised about local maxima of $|H(\omega)|$ and their position remains the same for all the successive sequences. It is easy to recognise that these regions coincides with the *ultrawide* band gaps. On the other, in the areas between the *ultrawide* gaps, we detect several smaller light blue regions which become more numerous and narrower at increasing index i. They are the standard band gaps whose 'evolution' is governed by the scaling feature described in Section 5. As expected, in all the plots shown in Fig. 11, no stop bands are found for $\rho_S/\rho_L = 1$, in which case both parts L and S are made up of the same material and then all rods from $\mathcal{F}_2$ to $\mathcal{F}_7$ are homogeneous.

Similarly to Fig. 11, the sector plots in Fig. 12 show the stop/pass band regions for periodic SMSs generated according to sequences from $\mathcal{F}_2$ to $\mathcal{F}_5$, assuming $l_L/l_S = \sigma_g$. As just observed for GMSs, the regions occupied by the *ultrawide* band gaps are the same for all the sequences following $\mathcal{F}_4$, whereas standard band gaps become more numerous and narrower within them.

7 Conclusions

This work is concerned with the study of harmonic axial wave propagation in infinite waveguides constructed by repeating a bi-phase elementary cell composed of two building elements that are combined according to the generalised Fibonacci sequence. In particular, the class of *precious* mean quasicrystalline sequences has been thoroughly analysed. The core of the investigation has focused on the properties of the arrangements of stop and pass bands obtained in the same frequency interval for different indices of the se-

quence. The main outcome of the paper is the illustration of the role of an invariant function of the circular frequency, named the Kohmoto's invariant, in determining those properties.

More in detail,

– we have exploited a dynamical trace mapping procedure to reveal how the properties of the transfer matrices correlate to the graphical representation of the Kohmoto's invariant; on this manifold, different kinds of orbits have been classified;

– the dynamical trace mapping reveals the existence of a special class of quasicrystalline rods, named *canonical* structures, that display special conservation properties in the pass/stop band layout at well defined *canonical* frequencies;

– the linearisation of the dynamical trace mapping about characteristic periodic points explains the scaling and self-similarity features of the dynamic spectra and the stop and pass band diagrams at varying generation index;

– *ultrawide* band gaps in the spectra have been analysed.

The results achieved in this paper provide the necessary insight to start a research programme in quasicrystalline metamaterials. The established methodology will be extended to investigate the dynamics of quasicrystalline beams, plates and composite materials.

Acknowledgements. This project has received funding from the European Union's Horizon 2020 research and innovation programme under Marie Skodowska-Curie Actions COFUND grant SIRCIW, agreement No 663830.

Appendix A

Traces $\mathsf{tr}\,\boldsymbol{T}_i$ $(i = 0, \ldots, 5)$ of GMSs generated by two different *canonical* sequences are reported in Figs. 13 and 14. The traces associated with the initial point R_0 are reported in the first plot of both figures, and then the other graphs show the traces involved in $R_1 = (x_3, x_2, x_1)$. Fig. 13 is for $E_L = E_S$, $A_L = A_S$, $l_S/l_L = 1/2$, $\rho_L/\rho_S = 1/4$, $(l_S/l_L)\sqrt{Q_S/Q_L} = (l_S/l_L)\sqrt{\rho_S/\rho_L} = 1/4$, so that condition $(28)_2$ is verified. Fig. 14 is computed for $E_L = E_S$, $A_L = A_S$, $l_S/l_L = 1/2$, $\rho_L/\rho_S = 4$, $(l_S/l_L)\sqrt{Q_S/Q_L} = (l_S/l_L)\sqrt{\rho_S/\rho_L} = 1$, which verify condition $(28)_1$. Note that in this case, $\mathsf{tr}\,\boldsymbol{T}_0 = \mathsf{tr}\,\boldsymbol{T}_1$ for each value of the dimensionless frequency. In both figures, *canonical* frequencies are marked by dot-dashed vertical lines.

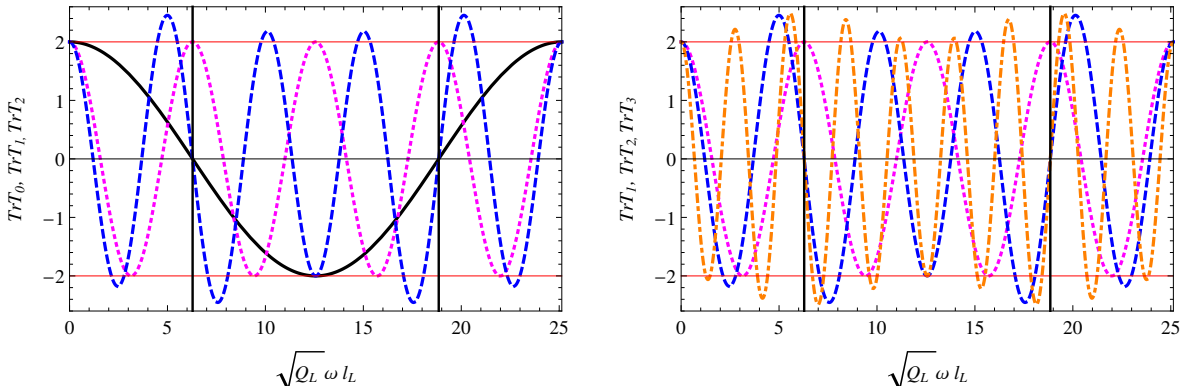

Figure 13: Plot of $\mathsf{tr}\,\boldsymbol{T}_i$ for GM *canonical* structures corresponding to $(l_S/l_L)\sqrt{Q_S/Q_L} = (l_S/l_L)\sqrt{\rho_S/\rho_L} = 1/4$ vs dimensionless frequency. On the left, $\mathsf{tr}\,\boldsymbol{T}_0$ (black solid line), $\mathsf{tr}\,\boldsymbol{T}_1$ (magenta dotted line) and $\mathsf{tr}\,\boldsymbol{T}_2$ (blue dashed line) are reported. On the right, $\mathsf{tr}\,\boldsymbol{T}_1$ (magenta dotted line), $\mathsf{tr}\,\boldsymbol{T}_2$ (blue dashed line) and $\mathsf{tr}\,\boldsymbol{T}_3$ (orange dash-dotted line) are displayed. The black vertical lines indicate the *canonical* frequencies.

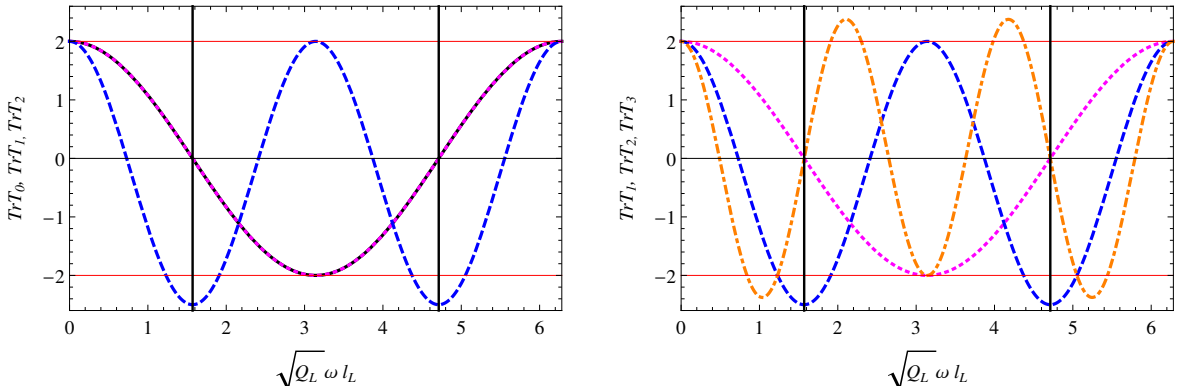

Figure 14: Plot of $\mathsf{tr}\boldsymbol{T}_i$ for GM *canonical* structures corresponding to $(l_S/l_L)\sqrt{Q_S/Q_L} = (l_S/l_L)\sqrt{\rho_S/\rho_L} = 1$ vs dimensionless frequency. On the left, $\mathsf{tr}\boldsymbol{T}_0$ (black solid line), $\mathsf{tr}\boldsymbol{T}_1$ (magenta dotted line) and $\mathsf{tr}\boldsymbol{T}_2$ (blue dashed line) are reported. On the right, $\mathsf{tr}\boldsymbol{T}_1$ (magenta dotted line), $\mathsf{tr}\boldsymbol{T}_2$ (blue dashed line) and $\mathsf{tr}\boldsymbol{T}_3$ (orange dash-dotted line) are displayed. The black vertical lines indicate the *canonical* frequencies.

Appendix B

Plot of functions $\kappa_g^+(\omega)$ and $\kappa_g^-(\omega)$ are reported in Fig. 15 for $l_S = l_L/\sigma_g$ and $\rho_S = \rho_L/2$. We note that both κ_g^+ and κ_g^- are characterised by small oscillations and that $\kappa_g^+ \gg 1 \gg \kappa_g^-$ for any frequency.

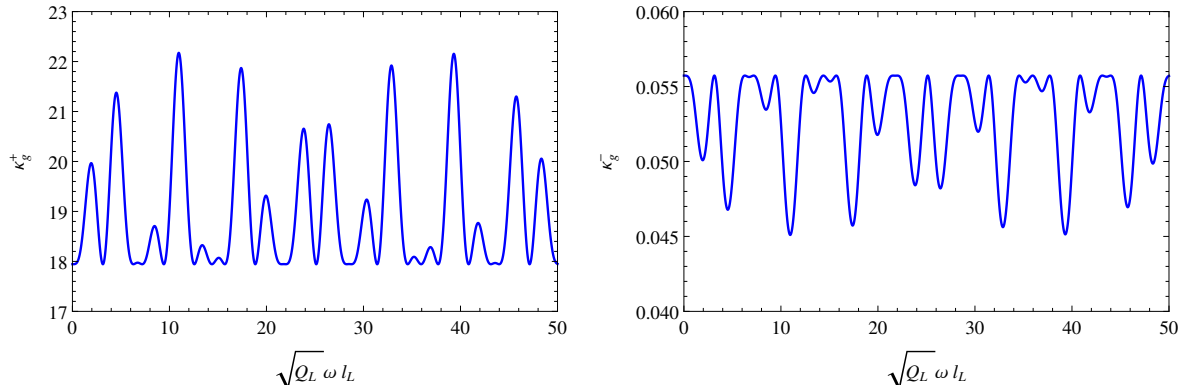

Figure 15: Plot of functions $\kappa_g^+(\omega)$ and $\kappa_g^-(\omega)$ in a graph where the abscissa reports the dimensionless frequency $\sqrt{Q_L}\omega l_L$. The calculations are for $l_S = l_L/\sigma_g$ and $\rho_S = \rho_L/2$.

References

Arnold, V., 1989. Mathematical Methods of Classical Mechanics. Springer-Verlag, New York.

Brun, M., Guenneau, S., Movchan, A., 2009. Achieving control of in-plane elastic waves. Appl. Phys. Lett. 94, 061903.

Brun, M., Guenneau, S., Movchan, A., Bigoni, D., 2010. Dynamics of structural interfaces: filtering and focussing effects for elastic waves. J. Mech. Phys. Solids 58, 1212–1224.

Carta, G., Brun, M., 2015. Bloch-Floquet waves in flexural systems with continous and descrete elements. Mech. Mater. 87, 11–26.

Colquitt, D., Brun, M., Gei, M., Movchan, A., Movchan, N., Jones, I., 2014. Transformation elastodynamics and cloaking for flexural waves. J. Mech. Phys. Solids 72, 131–143.

Colquitt, D., Colombi, A., Craster, R., Roux, P., Guenneau, S., 2017. Seismic metasurfaces: Sub-wavelength resonators and Rayleigh wave interaction. J. Mech. Phys. Solids 99, 379–393.

Ewing, M., Jardetzky, W., Press, F., 1956. Elastic waves in layered media. McGraw-Hill.

Farhat, M., Guenneau, S., Enoch, S., Movchan, A., 2009. Cloaking bending waves propagating in thin elastic plates. Phys. Rev. B 79, 033102.

Gei, M., 2010. Wave propagation in quasiperiodic structures, stop/pass band distribution and prestress effects. Int. J. Solids Struct. 47, 3067–3075.

Graff, K., 1975. Wave motion in elastic solids. Oxford University Press.

Gumbs, G., Ali, M., 1988. Dynamical maps, Cantor spectra and localization for Fibonacci and related quasiperiodic lattices. Phys. Rev. Lett. 60, 1081–1085.

Holzer, M., 1988a. Nonlinear dynamics and localization in a class of one-dimensional quasicrystals. Phys. Rev. B 38, 5756–5760.

Holzer, M., 1988b. Three classes of one-dimensional two-tile Penrose tilings and the Fibonacci Kronig-Penney model as a generic case. Phys. Rev. B 38, 1709–1720.

Huang, Z., Gumbs, G., Kolar, M., 1992. Localization in one-dimensional Thue-Morse chains. Phys. Rev. B 46, 479–486.

King, P., Cox, T., 2007. Acoustic band gaps in periodically and quasiperiodically modulated waveguides. J. Appl. Phys. 102, 014902.

Kohmoto, M., Kadanoff, L., Tang, C., 1983. Localization problem in one dimension: mapping and escape. Phys. Rev. Lett. 50, 1870–1872.

Kohmoto, M., Oono, Y., 1984. Cantor spectrum for an almost periodic Schroedinger equation and a dynamical map. Phys. Lett. 102A, 145–148.

Kohmoto, M., Sutherland, B., Iguchi, K., 1987. Localization in optics: quasiperiodic media. Phys. Rev. Lett. 58, 2436–2438.

Kolar, M., 1993. New class of one dimensional quasicrystals. Phys. Rev. B 47, 5498–5492.

Kolar, M., Ali, M., 1989a. Attractors of some volume-nonpreserving Fibonacci trace maps. Phys. Rev. A 39, 6538–6544.

Kolar, M., Ali, M., 1989b. Generalized Fibonacci superlattices, dynamical trace maps, and magnetic excitations. Phys. Rev. B 39, 426–432.

Kolar, M., Ali, M., 1990. One-dimensional generalized Fibonacci tilings. Phys. Rev. B 41, 7108–7112.

Kolar, M., Nori, F., 1990. Trace maps of general substitutional sequences. Phys. Rev. B 42, 1062–1065.

Kushwaha, M., Halevi, P., Dobrzynski, L., Djafari-Rouhani, B., 1993. Acoustic band structure of periodic elastic composites. Phys. Rev. Lett. 71, 2022–2025.

Laruelle, F., Etienne, B., 1988. Fibonacci invariant and electronic properties of GaAs/$Ga_{l\text{-}x}Al_xAs$ quasiperiodic lattices. Phys. Rev. B 37, 4816–4819.

Levine, D., Steinhardt, P., 1984. Quasicrystals: a new class of ordered structures. Phys Rev. Lett. 53, 2477–2480.

Lin, Y., 1962. Free vibrations of a continuous beam on elastic supports. Int. J. Mech. Sci. 4, 409–423.

Maldovan, M., 2013. Sound and heat revolutions in phononics. Nature 503, 209–217.

Milton, G., Briane, M., Willis, J., 2006. On cloaking for elasticity and physical equations with a transformation invariant form. New J. Phys. 8, 248.

Nemat-Nasser, S., Sadeghi, H., Amirkhizi, A., Srivastava, A., 2015. Phononic layered composites for stress-wave attenuation. Mech. Res. Comm. 68, 65–69.

Norris, A., 2008. Acoustic cloaking theory. Proc. Roy. Soc. A 464 (2097), 2411–2434.

Ott, E., 1993. Chaos in dynamical systems. Cambridge University Press.

Parnell, W., Norris, A., Shearer, T., 2012. Employing pre-stress to generate finite cloaks for antiplane elastic waves. Appl. Phys. Lett. 100, 171907.

Penrose, R., 1974. The role of aesthetics in pure and applied mathematical research. Bull. Inst. Maths. Appl. 10, 266–271.

Poddubny, A., Ivchenko, E., 2010. Photonic quasicrystalline and aperiodic structures. Physica E 43, 1871–1895.

Romeo, F., Luongo, A., 2002. Invariant representation of propagation properties for bi-coupled periodic structures. J. Sound Vib. 257, 869–886.

Shmuel, G., Pernas-Salomon, P., 2016. Manipulating motions of elastomer films by electrostatically-controlled aperiodicity. Smart Mater. Struct. 25, 125012.

Sigalas, M., Economou, E., 1992. Elastic and acoustic-wave band-structure. J Sound Vibr. 158, 377–382.

Steurer, W., 2004. Twenty years of structure research on quasicrystals. Part I. Pentagonal, octagonal, decagonal and dodecagonal quasicrystals. Acta Crystals 219, 391–446.

Steurer, W., Deloudi, S., 2008. Fascinating quasicrystals. Acta Crystals A64, 1–11.

Tamura, S., Nori, F., 1989. Transmission and frequency spectra of acoustic phonons in Thue-Morse superlattices. Phys. Rev. B 40, 9790–9801.

Willis, J. R., 2016. Negative refraction in a laminate. J. Mech. Phys. Solids 97, 10–18.

Wu, M.-L., Wu, L.-Y., Yang, W.-P., Chen, L.-W., 2009. Elastic waves band gaps of one-dimensional phononic crystals with functionally graded materials. Smart Mater. Struct. 18, 115013.

Zhao, M., Xie, Y.-Z., Zhang, X.-G., Gao, J., 2013. Band gaps of Lamb waves propagating in one-dimensional periodic and nesting Fibonacci superlattices thin plates. Thin Solid Films 546, 439–442.